Satellite-Based Characterization of Warm-Season Mesoscale Convective Systems over Southeastern Mainland China in Response to the Western Pacific Subtropical High

YIPENG HUANG,[a,b,c] MURONG ZHANG,[a,b] ZHIYONG MENG,[d] GUIXING CHEN,[e] AND YUCHUN ZHAO[b,c]

[a] *State Key Laboratory of Marine Environmental Science, Center for Marine Meteorology and Climate Change, College of Ocean and Earth Sciences, Xiamen University, Xiamen, China*
[b] *Xiamen Key Laboratory of Straits Meteorology, Xiamen Meteorological Bureau, Xiamen, China*
[c] *Key Laboratory of Straits Severe Weather, China Meteorological Administration, Fuzhou, China*
[d] *Department of Atmospheric and Oceanic Sciences, School of Physics, and China Meteorological Administration Tornado Key Laboratory, Peking University, Beijing, China*
[e] *School of Atmospheric Sciences, Sun Yat-sen University, Zhuhai, China*

(Manuscript received 8 March 2025, in final form 3 September 2025, accepted 18 September 2025)

ABSTRACT: Subtropical highs are large-scale dominant weather systems with significant impacts on regional climate and weather patterns. However, their cross-scale influence on mesoscale convective systems (MCSs) remains insufficiently understood. This study investigates how satellite-observed MCS characteristics vary with the western Pacific subtropical high (WPSH) over southeastern mainland China (SEMC), where the WPSH exerts a most frequent influence within the Asian continent. In 7-yr warm seasons, 725 WPSH days were identified and objectively classified into distinct weather types categorized as either WPSH-periphery or WPSH-center patterns, based on SEMC's location relative to the WPSH. Although MCSs are generally less frequent in the WPSH-center patterns than in the WPSH-periphery ones, their occurrence remains noteworthy near regional hotspots. Across all patterns, MCS occurrence consistently exhibits a diurnal peak in late afternoon and early evening. The WPSH-center patterns show a larger diurnal amplitude with more intensive MCS activity around this peak period. MCSs in the WPSH-center patterns tend to have shorter lifetimes, fewer merging/splitting processes, and a greater tendency to form locally over SEMC in the afternoon. Despite varying movement directions and orientations, MCSs across different patterns generally move along their orientation to facilitate the MCS "training" effect, especially in the WPSH-center patterns due to slower moving speeds and stronger intensities. The analysis on atmospheric conditions suggests that MCS occurrence in the WPSH-periphery patterns is more closely linked to synoptic disturbances, including enhanced moisture transport via low-level jet streams and mid-level upward motion. The convective parameters including convective available potential energy (CAPE), total column water, and K index effectively differentiate MCS-active days from MCS-inactive days for each WPSH pattern.

SIGNIFICANCE STATEMENT: This study examines how mesoscale convective systems (MCSs) behave in response to variations in the western Pacific subtropical high (WPSH) over southeastern mainland China (SEMC). The results reveal distinct characteristics of MCSs occurring at the WPSH center versus its periphery over SEMC. MCSs at the WPSH center are overall less frequent than those at the periphery, but they exhibit a stronger diurnal cycle with more concentrated occurrence around the active period and a higher potential to produce localized heavy rainfall due to slower movement and stronger intensity. Unlike the WPSH-periphery patterns, MCSs at the WPSH-center patterns often occur in weak synoptic-forcing environments of poor predictability. These findings underscore the importance of accounting for MCSs in both WPSH scenarios in forecasting, particularly as the WPSH expands under global warming, influencing future MCS trends.

KEYWORDS: Convective storms/systems; Subtropical cyclones; Mesoscale systems; Satellite observations

1. Introduction

Mesoscale convective systems (MCSs) represent cloud systems with organized grouping of thunderstorms that span thousands of square kilometers (Schumacher and Rasmussen 2020). These cloud systems serve as a pivotal component of the global hydrologic cycle by contributing substantial rainfall, particularly in the tropics and subtropics, where they account for more than 50% of total rainfall (Feng et al. 2021; Nesbitt et al. 2006). In China, the annual top 10 most influential heavy rain events typically involve MCSs (Li et al. 2023). Beyond heavy rainfall and flash floods, MCSs are also responsible for a significant portion of severe weather hazards, including strong winds, hail, and lightning (refer to the review in Schumacher and Rasmussen 2020). Given their profound impact at both global and regional scales, MCSs have long been a focus of research within meteorological and hydrological communities (Houze 2018). Understanding the mechanisms that govern the behavior of MCSs is critical for improving weather forecasting, hazard warnings, and water resource management. This is particularly important as MCSs are projected to become more frequent and intense under future climate warming (Feng et al. 2016; Hu et al. 2020; Taylor et al. 2017).

For convective storms to grow upscale into MCSs, synoptic patterns often play a crucial role. In the midlatitude United

---

Denotes content that is immediately available upon publication as open access.

Corresponding author: Murong Zhang, mrzhang@xmu.edu.cn

DOI: 10.1175/JCLI-D-25-0133.1

States, a great portion of MCS occurrences is linked to midtropospheric troughs and surface fronts, which provide the necessary forcing for ascent and the transport of moist, unstable air (Peters and Schumacher 2014; Trier et al. 2014). Low-level jet streams, such as the Great Plains low-level jet, also enhance MCS activity by transporting abundant moisture downstream (Song et al. 2019). Similar synoptic patterns have been identified in other midlatitude MCS-active regions, including China, South America, Africa, and Australia (Laing and Fritsch 2000). In the tropics, MCSs are often embedded within the intertropical convergence zone (ITCZ) (Houze et al. 2015), the Madden–Julian oscillation (MJO) (Zuluaga and Houze 2013), and synoptic easterly waves (Mathon et al. 2002). Due to differences in synoptic patterns, distinct MCS characteristics emerge between midlatitude and tropical regions. Midlatitude MCSs are generally more intense, better organized, and predominately move eastward at a faster speed than tropical MCSs, although they occur less frequently (Feng et al. 2021; Schumacher and Rasmussen 2020). Subtropical regions, as intermediate zones between midlatitude and tropical areas, have received relatively less attention in MCS research. Subtropical MCSs exhibit more ambiguous features compared to those in other regions, highlighting the need for an in-depth understanding. This study thus focuses on the variations in MCS behavior over subtropical regions, with particular emphasis on the impact of subtropical highs, the dominant synoptic systems in these areas.

Subtropical highs are semipermanent anticyclonic circulation systems that typically take a zonal form and are located between 20° and 40° latitude in each hemisphere. These systems cover approximately 40% of Earth's surface, significantly modulating regional and even global climate and weather patterns (Cherchi et al. 2018). In the Northern Hemisphere, the centers of subtropical highs, often marked by the 5880-gpm isoline at 500 hPa, are primarily found over the North Pacific Ocean and the North Atlantic Ocean. The western part of the North Pacific subtropical high, known as the western Pacific subtropical high (WPSH), exerts the most significant influence on flooding and drought conditions in East Asia, including China. The WPSH position and intensity largely determine the seasonal and intraseasonal variations of the East Asian monsoon rain belts (Ding and Johnny 2005; Guan et al. 2019). In most years, the monsoon rain belts undergo two distinct northward migrations, which correspond closely with the two northward shifts of the WPSH in mid-June and mid–late July (Su and Xue 2015). Anomalous WPSH activity can lead to extreme weather events in East Asia, such as the record-breaking heat waves in northeast Asia in 2018 (Liu et al. 2019) and the "super mei-yu" event in the central-eastern China in 2020 (Ding et al. 2021).

In addition to its well-known impacts on large-scale climate and weather, the cross-scale influence of WPSH on mesoscale weather processes, including MCSs, has garnered increasing attention. Severe convective activities are often observed at the WPSH's northwestern periphery, producing high-impact weather over southeastern China. Notable examples include the convection outbreak on 6 May 2020, which generated dense hail reports (Huang et al. 2022b), and the MCSs that caused record-breaking rainfall on 7 May 2018 (Huang and Zhang 2022). In these instances, the WPSH creates favorable conditions for convection development on its northwestern periphery, by guiding southerly warm air to interact with northerly cold air or by facilitating moisture transport from the ocean via southerly jet streams. Recent studies have also shown that an enhanced WPSH promotes the daytime accumulation of moist static energy within its core, which is then discharged at its northwestern periphery at night (Zeng et al. 2019). Additionally, it modulates the diurnal variation of low-level winds, enhancing nocturnal low-level jets (Zeng et al. 2022). These processes contribute to MCS activity and associated heavy rainfall outside the WPSH. However, most of these studies focus on case analyses of MCSs occurring at the WPSH periphery. There is a lack of comprehensive understanding regarding how MCSs respond to the variations in the WPSH pattern, particularly in terms of differences between MCSs that occur within and outside the WPSH.

A major reason for the knowledge gap regarding MCSs within subtropical highs can be attributed to the classical view that the center of subtropical highs is dominated by subsidence motion (e.g., Peixóto and Oort 1984), making these regions traditionally considered unfavorable for convection. However, some studies have highlighted that upward motion can also occur within subtropical highs, for example, in the western part of WPSH (Feng and Fu 2009; He et al. 2001), creating conditions that allow for cloud and precipitation development. Climatological studies based on 10-yr data show that during the boreal summer, the average cloud cover in the core regions of subtropical highs exceeds 30% (Feng et al. 2011), and the subtropical high precipitation contributes over 50% of local total rainfall (Feng and Fu 2009). In operational forecasting over eastern China, severe convective storms producing hazardous weather often occur under the WPSH. These events pose huge forecasting challenges due to the lack of synoptic-scale forcing as observed in the WPSH-periphery scenario (e.g., Lan et al. 2022; Yin and Cao 2010). Despite these findings, the general characteristics of well-organized MCSs within subtropical highs, and how they differ from those occurring outside these highs, remain largely unexplored.

Several studies focusing on the southeastern United States have found that regional precipitation is greatly modulated by the position of the North Atlantic subtropical high (Li et al. 2012; Nieto Ferreira and Rickenbach 2020). These studies revealed that domain-averaged precipitation was highest when the western ridge of the subtropical high was located southwest of its mean position and lowest when it was situated northwest. However, these studies mainly focused on regional precipitation characteristics, without delving into the details of MCS characteristics. To address this gap, the present study aims to examine the general features of warm-season MCSs in response to variations in the WPSH pattern, based on multiyear satellite observations. Special attention is given to the distinction between the WPSH center and periphery. The study focuses on southeastern mainland China (SEMC), a region most frequently affected by the WPSH within the Asian continent. The case analysis has shown MCSs in this region are often WPSH-involved and can contribute over 80% of the extreme rainfall total (Huang and Zhang 2022). The goal is to establish a cross-scale connection between the WPSH and MCSs over SEMC

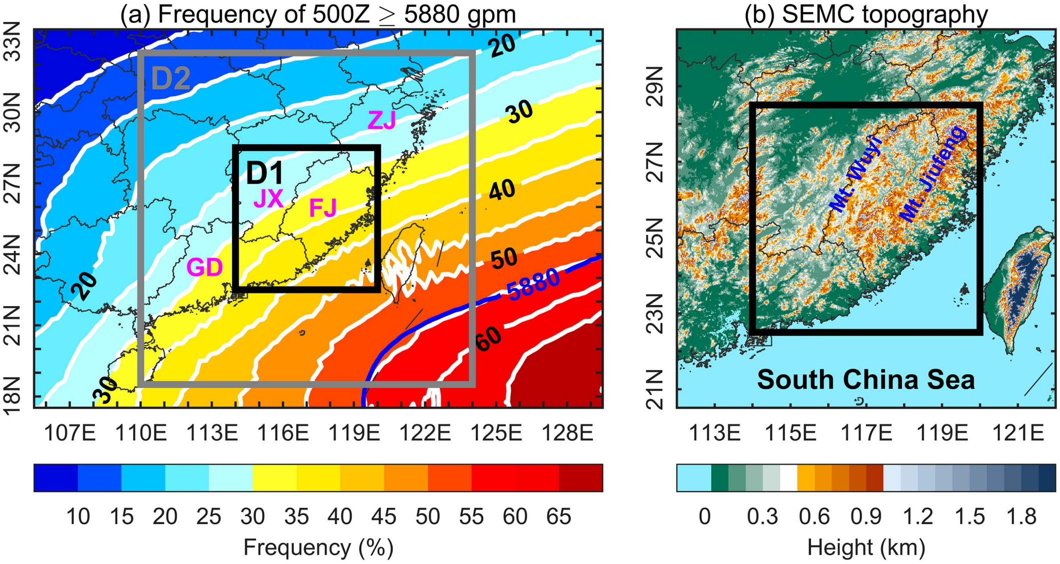

FIG. 1. (a) Occurrence frequency of ≥5880-gpm geopotential height at 500 hPa during April–September of 2016–22 over southern China, including the study domain, SEMC. (b) Topographic map of SEMC. Provincial boundaries are shown by gray curves in both (a) and (b). In (a), SEMC and its surrounding buffer domain are indicated by black and gray boxes, labeled as D1 and D2, respectively. The blue contour line in (a) represents the composite 5880-gpm isoline at 500 hPa over the same period. Magenta text labels SEMC-related provinces, including FJ, JX, GD, and ZJ. The black box in (b) highlights SEMC. The blue text in (b) identifies the two highest mountains within SEMC: Wuyi Mountains and Jiufeng Mountains.

from a climatological perspective, enhancing our understanding and forecasting capabilities for MCSs under different subtropical high patterns.

Section 2 outlines the data and methods used in this study. The typical synoptic patterns associated with the WPSH are presented in section 3. Section 4 describes the general features of MCSs under different WPSH synoptic patterns, while section 5 discusses the environmental factors that favor MCS development in each synoptic pattern. Finally, a summary and discussion are provided in section 6.

2. Data and methodology

a. *Himawari-8 satellite data, ERA5 reanalysis, and tropical cyclone database*

Infrared imagery derived from the Advanced Himawari Imager (AHI) onboard the *Himawari-8* satellite was used to identify and track MCSs. As a frontrunner among the new-generation geostationary meteorological satellites in the world, *Himawari-8* was launched on 7 October 2014 and was positioned at 140.7°E, providing a good field of view of East Asia (Bessho et al. 2016). After operating continuously since 7 July 2015, *Himawari-8* completed its mission on 13 December 2022, offering the longest sequence of observations among the new-generation geostationary satellites to date. To cover the entire warm season (April–September) over 7 years, this study utilized observations from 2016 to 2022. Specifically, the brightness temperature (BT) data from the 10.4-μm infrared band were employed, as this band is available both day and night with a scan interval of 10 min and a time coverage of 97.8% during the study period. This band has a spatial resolution of 2 km at nadir, and the data were interpolated into 0.02° longitude–latitude grids for the analysis.

We also utilized the fifth generation ECMWF atmospheric reanalysis (ERA5; Hersbach et al. 2020) for synoptic pattern classification and environmental condition diagnosis. ERA5 provides hourly data with a horizontal resolution of 0.25° × 0.25° at both surface and pressure levels. The ERA5 variables used in this study include geopotential height, temperature, wind, specific humidity, vertical velocity w, convective available potential energy (CAPE), total column water (TCW), and K index (KI). Equivalent potential temperature θ_e and the horizontal gradient of smoothed θ_e (to represent frontogenesis; Thomas and Schultz 2019) were also computed based on the ERA5 variables.

The China Meteorological Administration (CMA) tropical cyclone best track dataset (Lu et al. 2021) was used to exclude days associated with tropical cyclone activities. This dataset covers tropical cyclones that have developed over the western North Pacific since 1949, providing track information at 6-h intervals.

b. *Domain of interest*

The study domain, SEMC, spans 22.5°–28.5°N and 114°–120°E, encompassing most of Fujian (FJ) and Jiangxi (JX) provinces, eastern Guangdong (GD) province, and a small portion of southern Zhejiang (ZJ) province (Fig. 1a). Within mainland China, this region experiences the highest occurrence frequency of ≥5880-gpm geopotential height at 500 hPa during the study period, with values generally exceeding 25% and reaching up to 45% in the southeastern part (Fig. 1a). This indicates that the WPSH frequently affects SEMC during the warm season, potentially shaping different atmospheric patterns linked to WPSH intensity and position. The region also features complex terrain (Fig. 1b), including land–sea contrast and hills and mountains, which may affect MCS activity. For MCS tracking, as well as the selection and classification of WPSH days, a larger buffer domain was used, extending 4° beyond SEMC (i.e., 18.5°–32.5°N, 110°–124°E; the outer box in Fig. 1a).

c. *Selection and classification of WPSH days*

The WPSH is commonly defined by the 5880-gpm isoline at 500 hPa in both previous literature (e.g., Guan et al. 2019; Ren et al. 2013) and weather operation in China. We adopted the definition in this study and classified a day over SEMC as WPSH day if more than one-eighth of the buffer domain was occupied by the 5880-gpm isoline at 500 hPa at 0000 UTC (as a representative time of a day). When this ratio exceeds one-eighth, SEMC is either directly under the influence of the WPSH or located at its periphery. Additionally, approximately one-eighth of the buffer domain exhibits a WPSH occurrence frequency of over 50% (Fig. 1a), ensuring a sufficient number of WPSH days during the warm seasons. To focus specifically on the WPSH impact, we excluded days with tropical cyclone activity within the buffer domain, using the CMA best track dataset for this purpose.

This study objectively classified the synoptic patterns of WPSH days using the obliquely rotated principal component analysis method in the T mode (T-PCA; Huth 1993). In the T mode, the input data matrix is organized with grid points in rows and cases (time realizations) in columns, facilitating the efficient identification of typical synoptic patterns. Huth et al. (2008) demonstrated that T-PCA outperforms other objective classification techniques by accurately reproducing predefined dominant weather patterns and generating classification results that are less sensitive to preset parameters while maintaining good temporal and spatial stability. Previous studies have successfully applied T-PCA in various regions of China (e.g., Bai et al. 2021; Huang et al. 2022a; Wang et al. 2021). Following these studies, T-PCA was conducted using the open-source software "cost733class," developed under the COST Action 733 framework on "Harmonisation and Applications of Weather Type Classifications for European Regions" (Philipp et al. 2016). For synoptic pattern classification, the distribution of geopotential height at 500 hPa over the buffer domain at 0000 UTC during WPSH days was used.

d. *MCS defining and tracking*

Infrared imagery from geostationary satellites, with frequent refresh rates, has long been used for detecting MCSs. Satellite observations provide broad spatial coverage in a unified viewpoint, enabling robust MCS identification under diverse meteorological conditions (Vila et al. 2008). This contrasts with ground-based radars, which have limited detection ranges and spatial sampling inconsistencies. Compared to satellite precipitation products, next-generation geostationary satellites (e.g., *Himawari-8*) offer superior spatiotemporal resolution for cloud-based MCS tracking. Infrared data also avoid known precipitation underestimation issues in regions like SEMC (Shen et al. 2010). This study applied the method described in Huang and Zhang (2022) to identify and track MCSs, using infrared imagery from the *Himawari-8* satellite.

Following previous works (e.g., Chen et al. 2019), MCSs were defined as contiguous cold cloud clusters with infrared BTs lower than 235 K, an area larger than 1000 km^2, and a duration longer than 3 h. Sensitivity experiments on different combination of BT (230, 235, and 240 K) and area (100, 1000, and 10 000 km^2) thresholds were carried out to investigate the result uncertainties. It turns out all the tests display similar patterns of MCS occurrence in terms of both the spatial distribution and diurnal variation, despite with varying magnitude (figures not shown). These qualitatively consistent patterns confirm the robustness of our core findings to threshold selection.

MCS identification and tracking follows several procedures. First, potential MCS samples satisfying the BT and area thresholds were identified in each *Himawari-8* infrared image. A common automated tracking approach—the area overlap method—was then employed to track these samples across successive images. Potential samples in successive 10-min images were regarded as the same cloud cluster when their overlapping rate exceeded 15%. Only clusters persisting more than 3 h were designated as MCSs, with their corresponding samples retained for the analysis. The "formation (dissipation)" of MCS was defined when an MCS sample had no MCS sample overlap in the previous (next) satellite image. MCSs were considered to undergo a "merging (splitting)" process if they had more than one MCS sample overlap in the previous (next) satellite image, while a "continuity" process was defined by only one MCS sample overlap. To focus on regional characteristics, only MCSs with their centroid within SEMC during their life cycle (at least once) were retained for further analysis.

During the identification and tracking process, several MCS traits were collected, including size, eccentricity, orientation, motion, and intensity. MCS size was determined by counting covered satellite pixels (each representing approximately 4 km^2) belonging to an MCS sample. Eccentricity, reflecting the shape of MCS, was calculated as the ratio of the minor axis to the major axis of the ellipse that best fitted an MCS sample (Jirak et al. 2003). Orientation was defined as the counterclockwise angle between the east–west direction and the major axis of the best-fit ellipse. MCS motion was derived from the displacement of MCS samples belonging to the same MCS across successive satellite scans. The intensity of MCS was estimated using BTs, where lower BT values signify more intense MCS (Huang and Zhang 2022).

3. Synoptic patterns of WPSH days

A total of 725 WPSH days were identified, accounting for 56.6% of the seven warm seasons (1281 days). Synoptic circulations on these WPSH days were classified into five typical types, labeled T1–T5, in descending order of occurrence frequency (Figs. 2a,e–h). Each type is characterized by a distinct position of the WPSH center relative to SEMC: southeast (T1), northeast (T2), north (T3), east (T4), and northwest (T5).

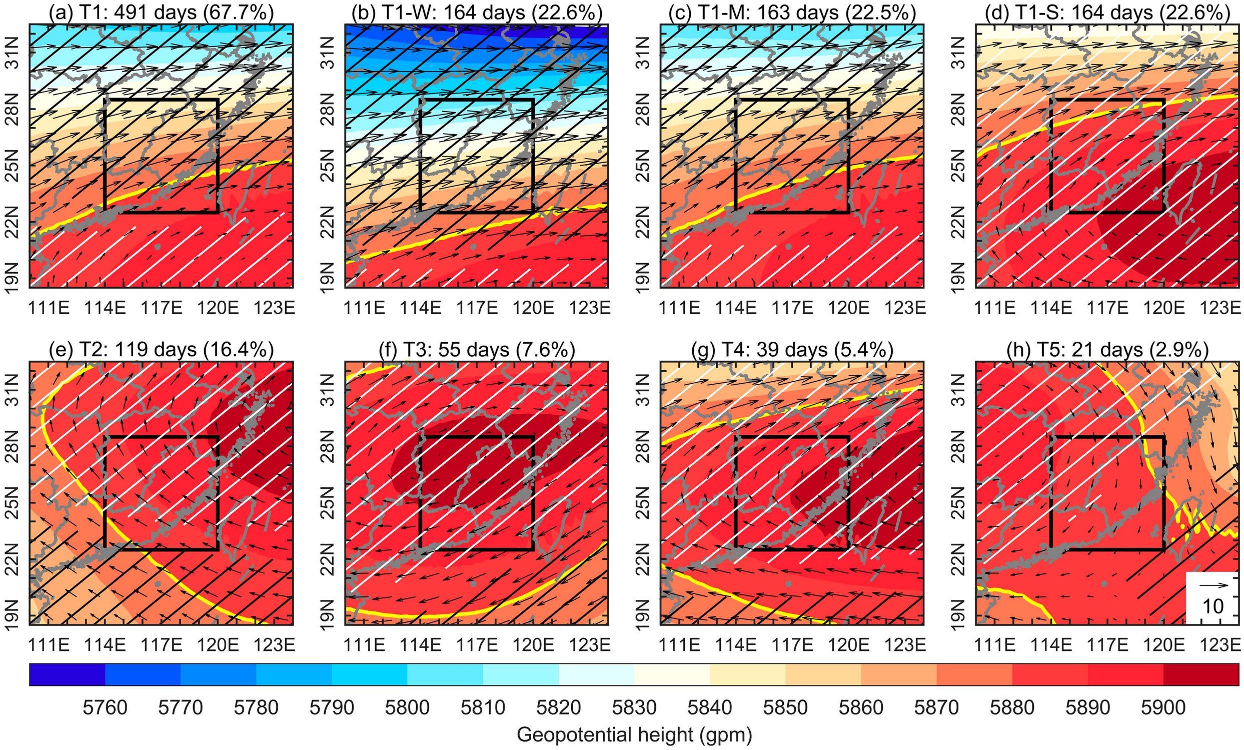

FIG. 2. Typical synoptic types of the WPSH days for SEMC during April–September of 2016–22, showing the composite 500-hPa geopotential heights (shading; gpm) and 500-hPa winds (vector; m s^{-1}) at 0800 LST. The number of days for each type is provided above the panel, along with its proportion relative to the total number of WPSH days. Provincial boundaries are indicated by gray curves, and the black box highlights SEMC. The yellow contour line represents the composite 5880-gpm isoline at 500 hPa. The white (black) hatched areas in each panel show where the composite geopotential heights are significantly higher (lower) than the mean state of all WPSH days, as determined by the Student's *t* test at a 90% confidence level.

SEMC is mostly covered by the 5880-gpm isoline in all synoptic types except T1 (Figs. 2a,e–h). Upon examining the mean 500-hPa geopotential height over SEMC, we found that the daily values exhibit a much wider range in T1 compared to the other four types (Fig. 3a). This suggests that SEMC may have varying distances to the WPSH center in T1, even though the center remains consistently located to the southeast. Given that T1 accounts for the predominant percentage (67.7%) of all WPSH days, we further divided T1 into three equal subtypes based on the daily mean 500-hPa geopotential height (Fig. 3a). The three subtypes, representing relatively weak, moderate, and strong WPSH intensity over SEMC, are labeled T1-W, T1-M, and T1-S, respectively (Figs. 2b–d). The mean 500-hPa geopotential heights in T1-W and T1-M are less than 5880 gpm, while those in T1-S are generally higher than 5880 gpm, similar to T2–T5 (Fig. 3a). The distribution of synoptic patterns shows clear intraseasonal variation (Fig. 3b). T1-W and T1-M are most common in early summer, with peaks in April and May, respectively, while T1-S tends to occur more frequently in June and September. As the WPSH migrates northward, T2–T5 become more prevalent in late summer from July to September, each peaking in different months.

Overall, T1-W and T1-M are types where SEMC is located on the northwest periphery of WPSH (i.e., WPSH-periphery types), while T1-S and T2–T5 are types where SEMC is directly impacted by the WPSH center (i.e., WPSH-center types) (Fig. 2). Compared to T1-M, T1-W is farther from the WPSH center and is characterized by stronger southwesterly winds over SEMC at 500 hPa (Figs. 2b,c). Among the WPSH-center types, the 500-hPa winds are relatively calm over SEMC, blowing mainly from the southwest in T1-S, southeast in T2, east in T3, south in T4, and north in T5 (Figs. 2d–h). At the midlevel, widespread upward motions (i.e., negative 500-hPa *w*) are observed over SEMC in the WPSH-periphery types, while in the WPSH-center types, the vertical motions become slightly upward (T1-S and T5) and even predominantly downward (T2–T4) (Fig. 4).

At mid–low tropospheric levels, southwesterly jets along the WPSH's northwestern periphery dominate the entire SEMC in the WPSH-periphery types, driving strong moisture fluxes across the region (Figs. 4a,b). These types also exhibit pronounced 700-hPa θ_e gradients over northern SEMC (Figs. 5a,b), indicating conditions favorable for frontogenesis. In contrast, the WPSH-center types feature much weaker synoptic-scale flows and moisture fluxes (Figs. 4c–g), warmer and moister environments with higher θ_e and reduced gradients (Figs. 5c–g). Moreover, vertical wind shear between the surface and 500 hPa (~0–6-km layer) is consistently stronger and predominantly westerly in the WPSH-periphery types, whereas the WPSH-

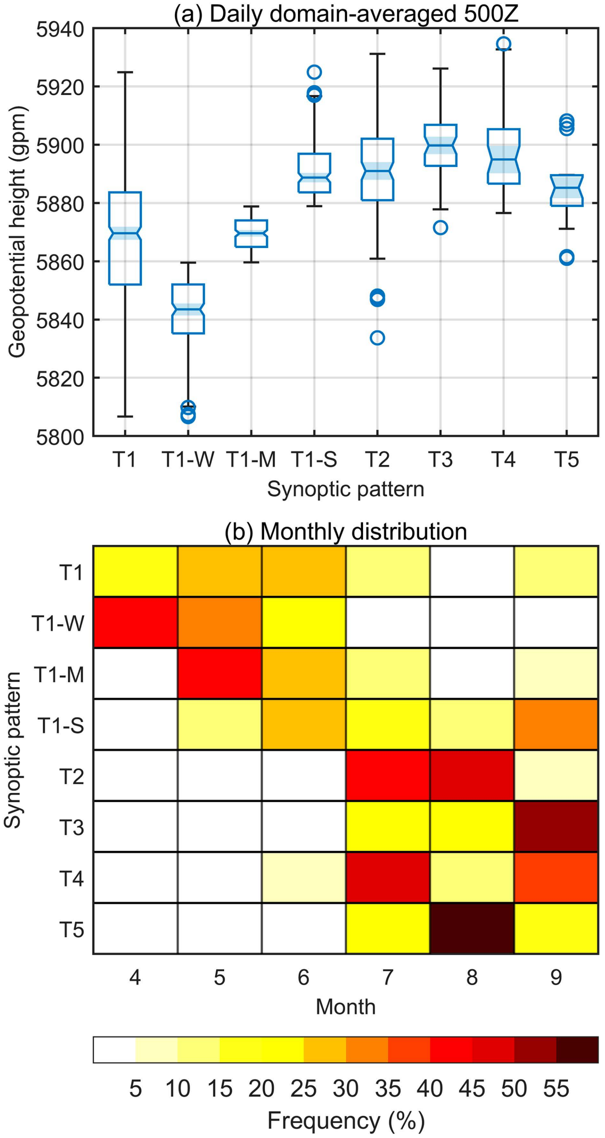

FIG. 3. (a) Box-and-whisker plots of daily 500-hPa geopotential heights averaged over the entire SEMC domain for different WPSH types. (b) Monthly variation in the occurrence frequency of WPSH days for each WPSH type. In (a), for each box-and-whisker plot, the top and bottom edges of the box represent the upper (q_3) and lower (q_1) quartiles, respectively. The line inside the box indicates the median. Sample outliers, denoted by circles, are values that exceed $q_3 + 1.5 \times (q_3 - q_1)$ or fall below $q_1 - 1.5 \times (q_3 - q_1)$. The whiskers above and below each box represent the nonoutlier maximum and minimum values, respectively.

center types exhibit weaker shear with more variable directions (Fig. 5). Collectively, these contrasts suggest that synoptic forcing is much more significant in the WPSH-periphery types than in the WPSH-center types.

4. General features of MCSs in different WPSH patterns

During the WPSH days of the seven warm seasons, a total of 3463 MCSs were identified over SEMC, with nearly 85 000 samples detected in the *Himawari-8* infrared images. Based on these samples, this section will present the general features of MCSs during the WPSH days, categorized according to different WPSH patterns. To enhance statistical significance in WPSH-periphery and WPSH-center comparison, T2–T5 were combined into a single WPSH-center pattern. This consolidation was justified by their lower occurrence frequency relative to the T1 subtypes, shared late-summer occurrence, and similar environmental conditions of weak synoptic forcing. Thus, we established four major WPSH patterns for following comparison: T1-W and T1-M representing WPSH-periphery scenarios versus T1-S and the combined T2–T5 representing WPSH-center scenarios.

a. *Spatial distribution*

During the WPSH days, MCS occurrence is most active over the north-central part of SEMC (Fig. 6a). The main hotspot is located between the Wuyi Mountains and Jiufeng Mountains, the two highest peaks in the region, with an occurrence frequency reaching up to 6%. A minor hotspot is observed in the southwestern part, though its frequency is below 5%. Notably, MCS activity is minimal over the sea, creating a pronounced offshore gradient in MCS frequency along the coastline.

The spatial distribution of MCS occurrence varies significantly across different WPSH patterns. Among the four patterns, T1-W most closely resembles the overall distribution but with a higher MCS frequency, reaching up to 8% over both hotspots (Fig. 6b). The widespread MCS occurrence could be attributed to the strong moisture fluxes (>80 g kg^{-1} m s^{-1}) over SEMC (Fig. 4a). The north-central MCS hotspot is largely associated with frontal systems, as indicated by strong θ_e gradients, while the southwest hotspot is more likely linked to a warm-sector regime, distant from the fronts and characterized by high θ_e (Fig. 5a). Previous studies have pointed out that frontal rainfall and warm-sector rainfall are two typical rainfall types in southern China during early summer, and both are largely driven by MCSs (Li and Du 2021; Wu et al. 2020; Zhang and Meng 2019; Zhang et al. 2022). This is confirmed by the MCS distribution here, particularly when the T1-W pattern is most prevalent during early summer. For example, on 7 May 2018, with a T1-W pattern, MCSs developed in a warm-sector environment near the southern hotspot, resulting in a record-breaking rainfall event (Huang and Zhang 2022). In T1-M, the MCS-active zone shifts northward, forming an arc that extends toward both the east coast and inland west, with a broad area exhibiting more than 8% frequency (Fig. 6c). This displacement corresponds to strong moisture fluxes confined to northern SEMC that result from the northward displacement of southwesterly jets along the advancing WPSH periphery relative to T1-W (Fig. 4b), as well as the concurrent northward shift of the frontogenesis zone with high θ_e gradients (Fig. 5b).

The WPSH-center patterns (i.e., T1-S, T2–T5) generally show a lower MCS frequency than the WPSH-periphery patterns (Fig. 6). However, MCS occurrence in these patterns should not

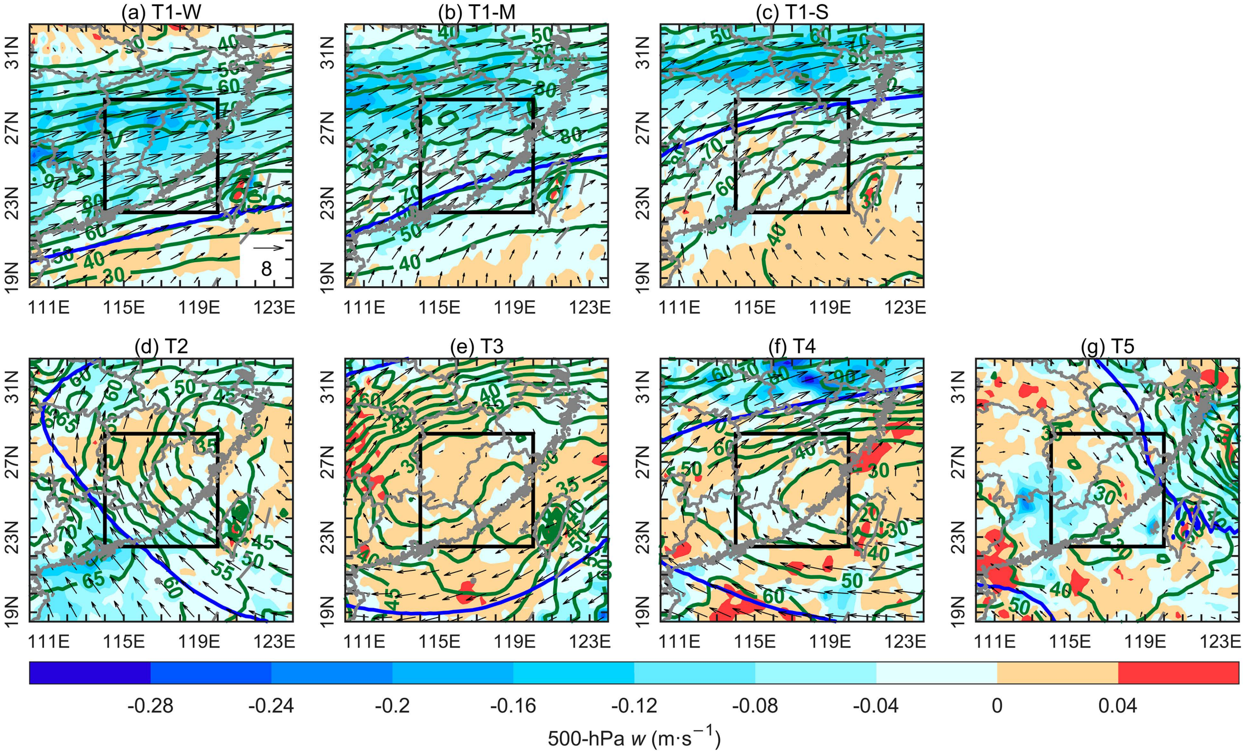
(a) T1-W (b) T1-M (c) T1-S (d) T2 (e) T3 (f) T4 (g) T5

FIG. 4. Composite environmental features for different WPSH types, showing 500-hPa vertical velocity (shading; m s^{-1}), 700-hPa moisture fluxes (contours; g kg^{-1} m s^{-1}), and 700-hPa winds (vectors; m s^{-1}). Provincial boundaries are outlined by gray curves. The black box denotes SEMC. The blue contour line indicates the composite 5880-gpm isoline at 500 hPa.

be overlooked, particularly over the hotspots. This is especially true for T1-S, where maximum MCS frequencies are up to 7%. These results support the idea that convective activities within the subtropical high centers may be more active than commonly thought, warranting closer attention. For the WPSH-center patterns, the MCS hotspot can occur in coastal areas or inland mountainous areas. Regardless, these patterns show a low frequency of MCS occurrence over the sea, consistent with the WPSH-periphery patterns. MCS development under the WPSH center may lack significant synoptic forcing and rely more on localized mechanisms to help the warm, humid air evolve into MCSs. As a result, the MCS distribution varies considerably across these patterns. This variability highlights the difficulty in forecasting and issuing warnings for MCSs in the WPSH-center regimes, where the absence of synoptic forcing makes prediction more challenging.

b. *Diurnal variation*

To investigate the diurnal cycle of MCS occurrence, MCS fraction was defined for each satellite scan as the ratio of MCS area to the total SEMC area. A higher MCS fraction indicates a larger MCS coverage over SEMC. For all WPSH days, MCS fraction tends to increase noticeably after midday, reaching its peak around 1800–1900 LST at nightfall, and then declines in the evening (Fig. 7a). On average, the diurnal amplitude of MCS fraction, defined as the difference between the maximum and minimum hourly means divided by the maximum hourly mean, is 76.2%.

For different WPSH patterns, the diurnal variation of MCS fraction similarly shows a single peak, with the peak hour ranging between 1600 and 1900 LST (Figs. 7b–e). However, the diurnal amplitude is much larger in T1-S and T2–T5 than in T1-W and T1-M, indicating a stronger diurnal cycle signal in the WPSH-center patterns. This suggests that MCS occurrence under the direct influence of WPSH is more likely tied to thermodynamic effects with a clear diurnal pattern. In contrast, MCS occurrence in the WPSH-periphery patterns is mainly driven by significant synoptic forcing, such as synoptic fronts, leading to less pronounced diurnal variation. The contrast in diurnal variation is also clearly reflected in the spatial distribution of MCS frequency every 3 h (Fig. A1 in appendix A).

The peak hour of MCS occurrence was further examined for different WPSH patterns in terms of spatial distribution [Figs. 8a(1)–d(1)]. It is evident that the offshore distribution of peak hours is more complex than inland, with a broader time span and more irregular patterns. This complexity arises from the low frequency of offshore MCSs, even during the peak hours [Figs. 8a(2)–d(2)], resulting in a more random distribution influenced by factors such as the offshore propagation of inland MCSs and local offshore MCS generation. In contrast, the inland peak hours are generally concentrated in the late afternoon to evening. For the three T1 subtypes, peak times progressively become later from southwest to northeast [Figs. 8a(1)–c(1)].

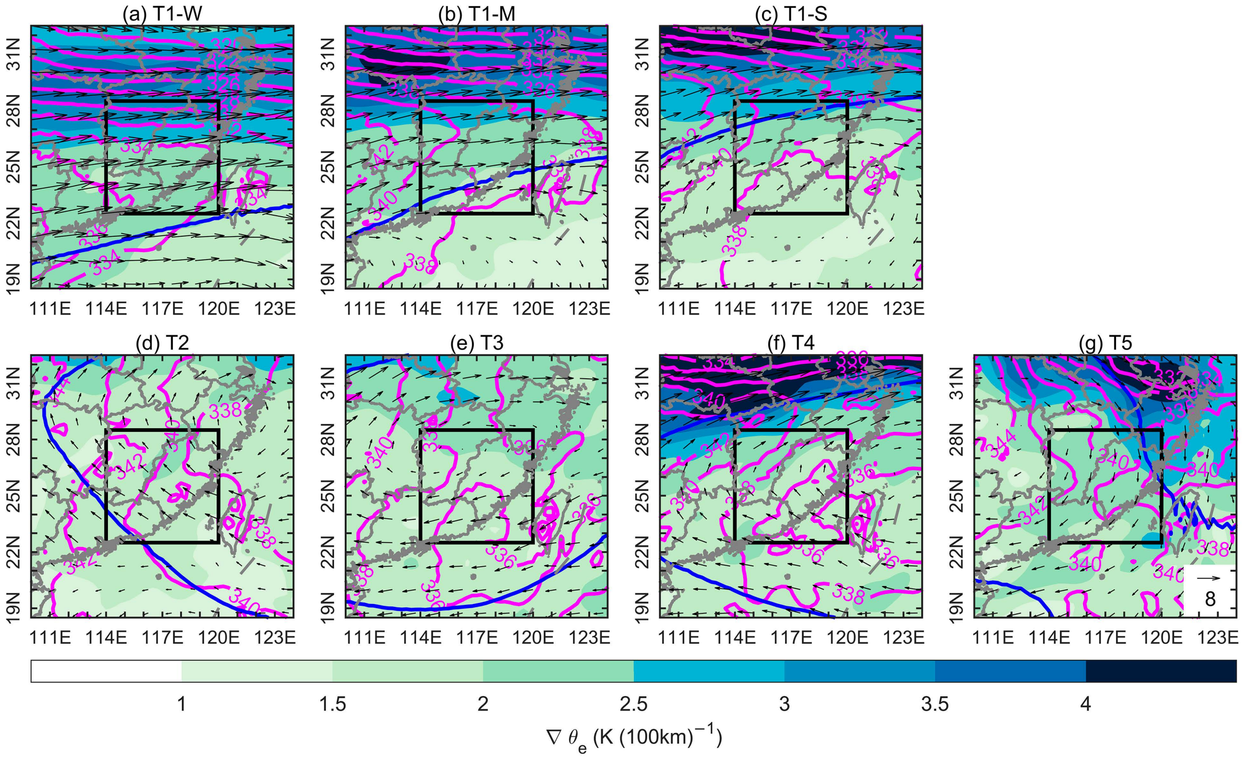

FIG. 5. Composite environmental features for different WPSH types, showing 700-hPa equivalent potential temperature (θ_e) (contours; K), horizontal gradient of smoothed 700-hPa θ_e [shading; K (100 km)$^{-1}$], and vertical wind shear between the surface and 500 hPa (vectors; m s^{-1}). Provincial boundaries are outlined by gray curves. The black box denotes SEMC. The blue contour line indicates the composite 5880-gpm isoline at 500 hPa.

This is likely linked to the eastward and northward propagation of MCS hotspots, particularly from the afternoon onward [Figs. A1a–c]. From T1-W to T1-M to T1-S, peak hours shift later, especially in northern SEMC. In contrast, T2–T5 exhibits less pronounced peak-hour variation [Fig. 8d(1)]. Nevertheless, a delayed peak from coastal regions (notably the southeast coast) to inland mountains remains evident, consistent with the northwestward migration of coastal MCS hotspots [Figs. A1d].

It is noteworthy that the peak frequencies in the WPSH-center patterns are comparable to, or even exceed (T1-S), those in the WPSH-periphery patterns [Figs. 8a(2)–d(2)]. This contrasts with the overall frequency results, where the WPSH-periphery patterns have higher frequencies (Fig. 6). This suggests that MCSs within the WPSH center tend to occur more intensively during specific time periods, especially around the peak time, rather than being distributed throughout the day. It is further supported by the relatively higher MCS fraction around the peak time in the WPSH-center patterns (Figs. 7b–e), as well as the prominent MCS frequency between 1500 and 2100 LST (Fig. A1). Figure B1 in appendix B exemplifies the evolution of MCSs occurring in the typical days of the WPSH-periphery and WPSH-center patterns, which also highlights a more concentrated MCS appearance between the late afternoon and early evening in the WPSH-center patterns.

c. *MCS stages during the life cycle*

This subsection compares the key stages of the MCS life cycle across different WPSH patterns. Of the 3463 identified MCSs, over 83% have their entire lifetime—from formation to termination—occurring within the same synoptic type, particularly within the three T1 subtypes (Fig. 9a). The remaining MCSs mostly transition between two synoptic types (16%), with only a small fraction experiencing three or four types. The dominance of MCSs remaining within a single synoptic type can be attributed to the relatively stable synoptic condition over short time scales, as well as the generally subdaily duration of MCS life cycle. To minimize cross-type interference, only MCSs that remain within a single synoptic type throughout their life cycle are included in the following comparison in this subsection.

MCS lifetime varies across synoptic patterns (Fig. 9b). The average MCS lifetimes range from approximately 5.9 to 7.1 h, consistent with previous studies (Yang et al. 2015). The longest average lifetime is observed in T1-W, where up to 20% of MCSs persist for more than 9 h, while the shortest lifetime is seen in T2–T5. Overall, MCSs under the WPSH-periphery patterns tend to have longer lifetimes than those under the WPSH-center patterns. Previous studies have indicated that the merging process between MCSs can contribute to their persistence (Huang and Zhang 2022), and our results confirm this, showing that

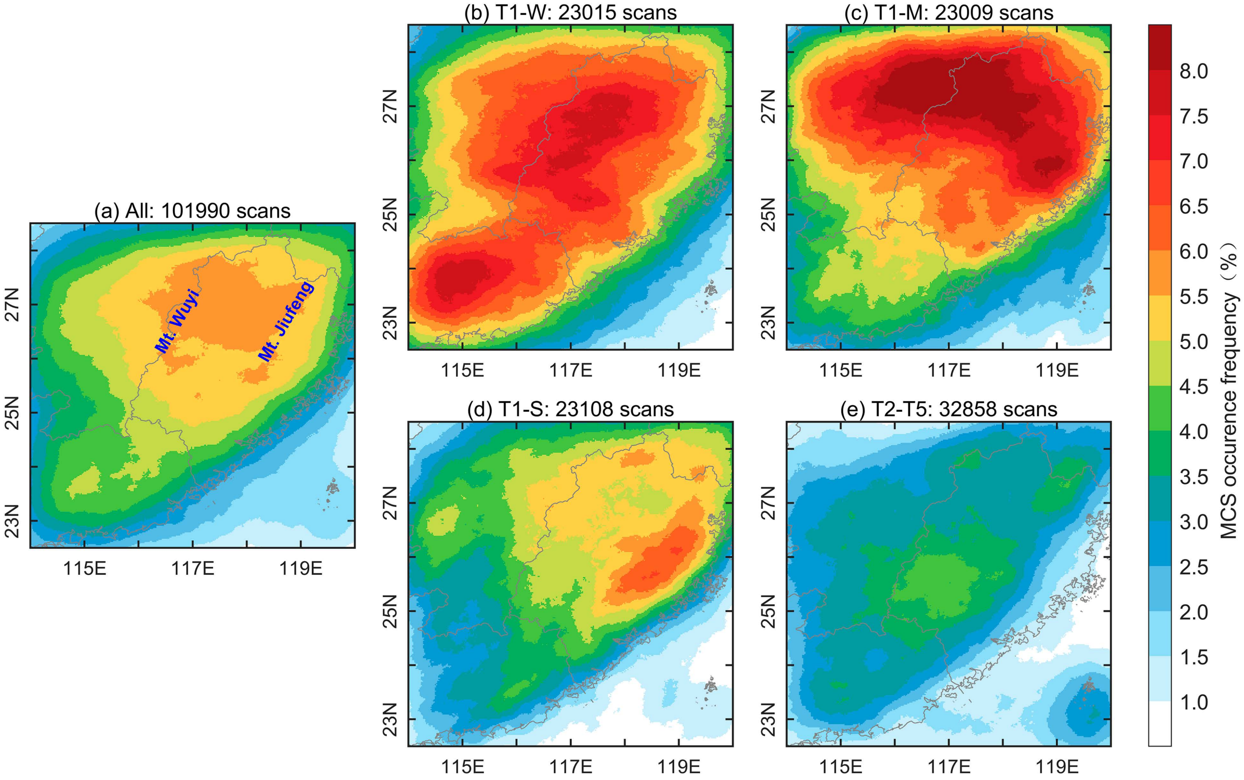

FIG. 6. Spatial distribution of MCS occurrence frequency for (a) all WPSH days and (b)–(e) different WPSH patterns. The number of *Himawari-8* satellite scans used to identify MCS objects is indicated above each panel for the corresponding pattern. Provincial boundaries are shown by gray curves. The blue text in (a) identifies the two highest mountains within SEMC: Wuyi Mountains and Jiufeng Mountains.

patterns with longer MCS lifetimes tend to have more frequent MCS merging events (Fig. 9c). Interestingly, the patterns with longer MCS lifetimes also exhibit more frequent occurrences of the MCS splitting process (Fig. 9d). This suggests that MCSs with longer lifetimes have a greater likelihood of splitting.

MCSs are observed to predominantly form and terminate in a natural way (without merging or splitting process) across all synoptic patterns (over 60%), despite the percentage varies between patterns (Figs. 9e,f). Overall, a higher proportion of MCSs forms and terminates naturally in the WPSH-center patterns compared to the WPSH-periphery patterns. In addition to natural processes, MCSs most commonly form through splitting and terminate through merging, which is most prominent in T1-W.

MCSs affecting SEMC can form and terminate either locally or elsewhere. Figure 10 illustrates the geographical distribution of MCS formation and termination sites. Compared to the WPSH-center patterns, the WPSH-periphery patterns show a higher proportion of MCSs forming outside SEMC, with the maximum percentage reaching ~45% in T1-W [Figs. 10a(1)–d(1)]. These MCSs generally originate to the west of SEMC and propagate into the region, especially in T1-W and T1-M, where westerly winds prevail. In the WPSH-periphery patterns, MCS formation sites within SEMC are distributed across the entire domain, whereas in the WPSH-center patterns, formation sites are more concentrated in the central mountainous regions, oriented from the southwest to northeast of SEMC. This suggests that orographic effects play a more significant role in MCS formation within the WPSH center. Additionally, the WPSH-periphery patterns exhibit a higher proportion of MCSs terminating outside SEMC, particularly to the east, compared to the WPSH-center patterns [Figs. 10a(2)–d(2)].

MCS formation exhibits more pronounced diurnal variation in the WPSH-center patterns than in the WPSH-periphery patterns (Fig. 11a). Approximately half of MCSs form in the afternoon (1200–1800 LST) in T1-S, with the percentage increasing to over 65% in T2–T5. In contrast, MCS formation in the WPSH-periphery patterns is more evenly distributed throughout the day, with the afternoon percentage around 40% in T1-M and less than 30% in T1-W. Regarding MCS termination, the WPSH-center patterns show a stronger diurnal signal than the WPSH-periphery types again, with more MCSs terminating during the night, especially between 1900 and 2300 LST (Fig. 11b).

d. MCS movement, morphology, and intensity

This subsection further compares several MCS traits across different WPSH patterns, including movement, morphology, and intensity—factors that have long been recognized as important in modulating MCS rainfall production. To avoid

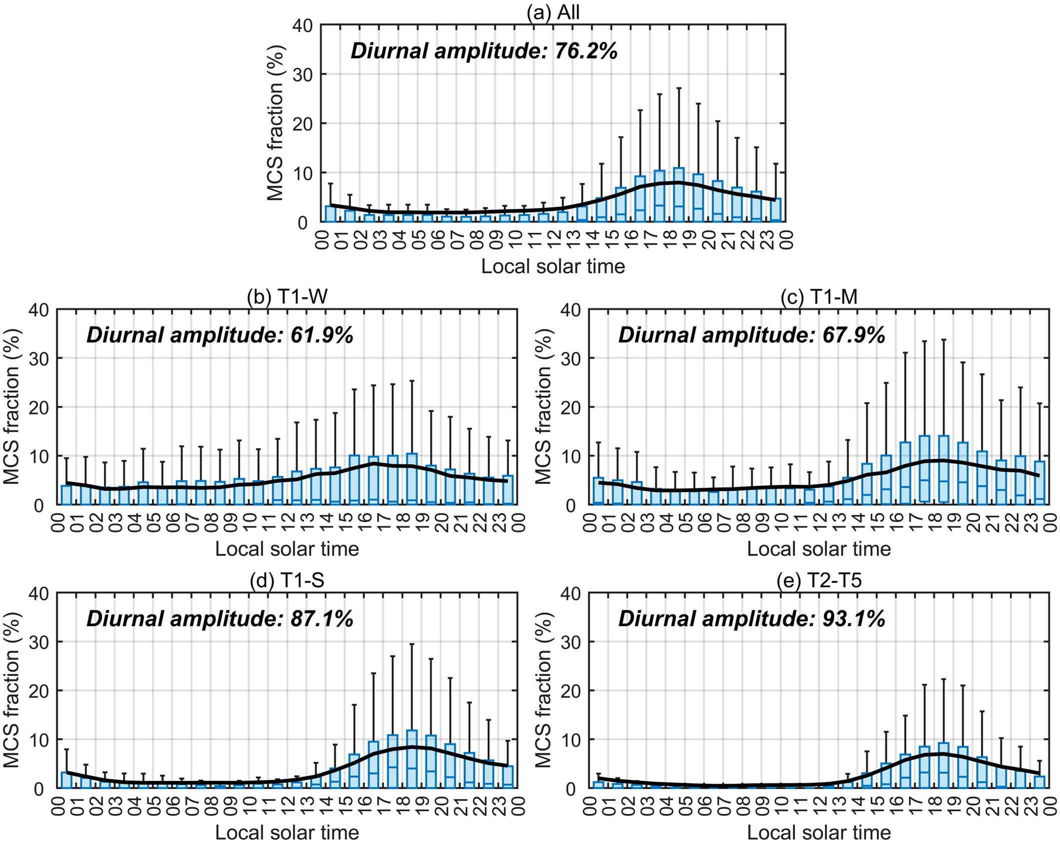

FIG. 7. Diurnal cycle of MCS fraction over SEMC for (a) all WPSH days and (b)–(e) different WPSH patterns. The hourly MCS fractions are shown in box-and-whisker plots (refer to Fig. 3 for the plot style). The mean MCS fractions for each hour are plotted as black lines. The diurnal amplitude of MCS fraction is given in the top-left corner of each panel.

anomalies caused by merging and splitting processes, only the MCS samples that follow a continuity process are included in the comparison.

It turns out that MCS motions vary significantly with WPSH patterns, primarily governed by the prevailing winds at midlevels. For the T1 subtypes, which are influenced by westerly flows (Figs. 2b–d), MCSs generally move eastward (Figs. 12a–c). As the westerly flows weaken from T1-W to T1-M to T1-S, the eastward component of motion decreases from 92.4% to 78.5% to 60.6% and the movement slows, particularly in the eastward direction. In T2–T5, where easterly or northerly flows dominate (Figs. 2e–h), MCS motions shift predominantly westward and southwestward (Figs. 12d). Overall, MCSs in the WPSH-periphery patterns move faster, with a median speed of 12.9 m s^{-1}, whereas those in the WPSH-center patterns move more slowly, with a median speed of 7.9 m s^{-1}. The T1, associated with the westerly jet, has the highest median moving speed of 16.2 m s^{-1}, which is comparable to the speed of squall lines (Meng et al. 2013). As noted by Feng et al. (2021), tropical and subtropical MCSs typically move westward at moderate speeds of 6–12 m s^{-1}, while mid- and high-latitude MCSs tend to move eastward at faster speeds of 12–26 m s^{-1}. Thus, MCSs in the WPSH-periphery patterns exhibit more mid- and high-latitude characteristics, while those in the WPSH-center patterns align more closely with tropical and subtropical MCS attributes.

The various WPSH patterns show no significant difference in MCS size, although the WPSH-center patterns have a slightly higher proportion of small-sized MCSs (Fig. 13a). As a key morphological parameter, eccentricity is commonly used to categorized MCSs into two types from a satellite view: 1) persistent elongated convective systems (PECSs; eccentricity < 0.7) and 2) mesoscale convective complexes (MCCs; eccentricity ≥ 0.7) (Jirak et al. 2003; Yang et al. 2015). The results reveal that about 80% of MCSs in each WPSH pattern are PECSs, with over half of them having a particularly linear shape (eccentricity < 0.5) (Fig. 13b).

Relative to MCS size and shape, MCS orientation shows more distinct variations among the WPSH patterns (Fig. 13c). From T1-W to T1-S, MCSs have more northeast–southwest orientation while less east–west orientation. This trend corresponds to the weakening westerly vertical wind shears (Figs. 5a–c). In the composite WPSH-center pattern (T2–T5) where the shears are weak and have less northeast–southwest component (Figs. 5d–g), MCSs become more east–west oriented and less northeast–southwest oriented compared to T1-S. Despite

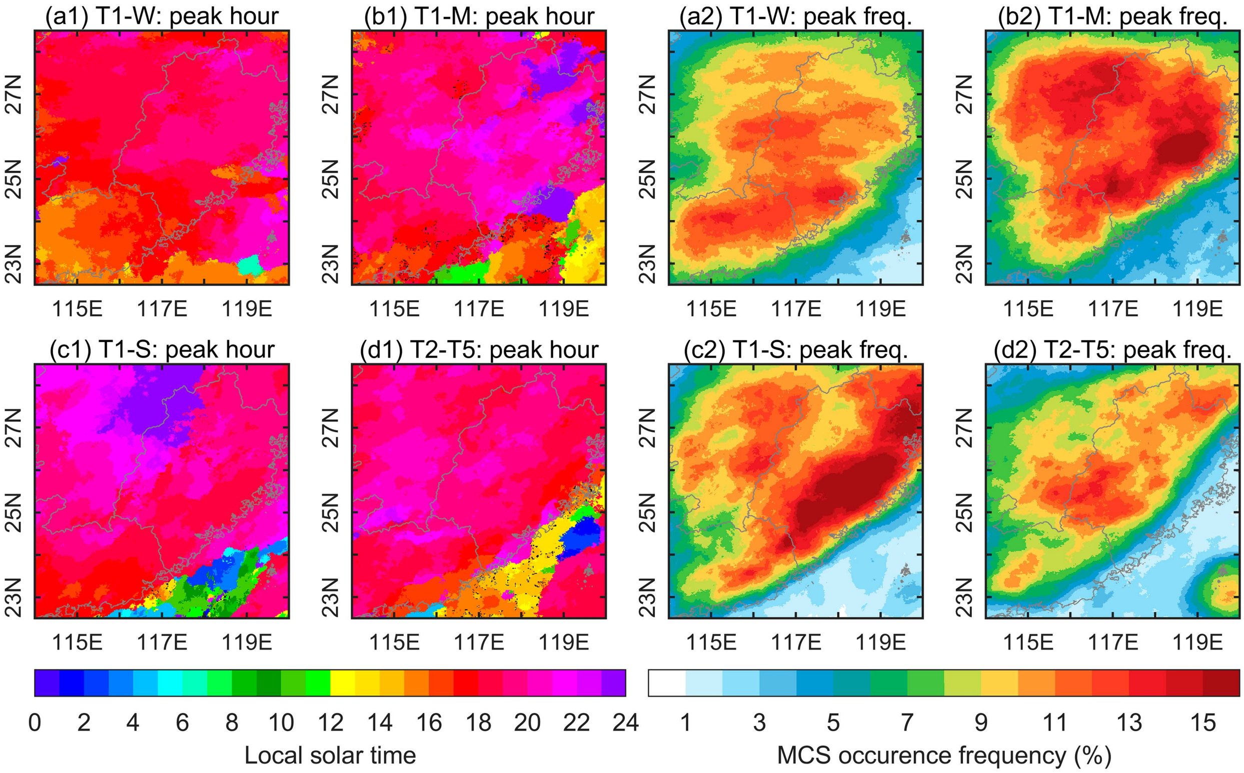

FIG. 8. Spatial distribution of (a1)–(d1) peak occurrence hour and (a2)–(d2) peak occurrence frequency of MCSs for different WPSH patterns. Provincial boundaries are denoted by gray curves. The black areas in (a1)–(d1) indicate regions where the peak occurrence frequency is zero, and therefore, the peak occurrence hour is unavailable.

significant variations in MCS orientation and movement direction across the patterns, the angle between them remains relatively constant, with a median of ∼30° and most samples under 45° in each pattern (Fig. 13d). For linear MCSs, this small angular offset promotes parallel movement of convective cells relative to the convective line, enabling repeated cell passages over the same area—a well-known MCS "training" effect that enhances heavy local rainfall production (Schumacher and Johnson 2005; Schumacher and Rasmussen 2020). This mechanism is particularly effective in the WPSH-center patterns, where slower MCS movement further facilitates the training effect (Huang and Zhang 2022).

MCS intensity is compared across different WPSH patterns using cloud-top BTs. For each MCS sample, the BTs of the 10% coldest MCS pixels are averaged to assess the MCS intensity. More intense MCSs, indicated by lower BTs, are observed in the WPSH-center patterns than in the WPSH-periphery patterns (Fig. 14a). Specifically, MCSs are weakest in T1-W and strongest in T2–T5, with median BTs of about 220 and 212 K, respectively. The WPSH-center patterns generally feature a warmer, moister, and more unstable environment, as shown by higher values of θ_e (Fig. 5) and daytime CAPE (refer to the 0800- and 1400-LST CAPE in Fig. 16a), which contribute to the intensity differences between patterns.

When examining the spatial distribution of extreme MCS intensity (i.e., the average of the 10% coldest MCS BTs for each pixel), we found that the overall weaker MCS intensity in T1-W is primarily due to weaker MCSs near the north-central hotspot associated with frontal systems (Fig. 14b). In contrast, the south hotspot, located in the warm sector, experiences much stronger MCSs with BTs about 8 K colder. This meridional intensity contrast is not observed in the other patterns (Figs. 14c–e). These patterns feature strong MCSs in both coastal and inland regions. The overall contrast in MCS intensity between the WPSH-periphery patterns and WPSH-center patterns can be partially revealed in the examples of T1-W and T5 in Fig. B1, with wider area of extreme cloud-top BTs colder than 190 K observed in the T5 case between 1600 and 2000 LST.

In summary, MCSs across different WPSH patterns show little variation in size and shape when viewed from satellite-observed cloud systems. However, MCS movement and orientation exhibit significant differences, depending on the prevailing environmental flows in each pattern. Notably, the concurrent changes in moving direction and orientation consistently form small angles between themselves, which are conducive to the MCS training effect in both WPSH-periphery and WPSH-center patterns. Compared to the WPSH-periphery patterns, the WPSH-center patterns feature slower-moving MCSs with stronger intensity. This suggests that MCS characteristics within the WPSH center might amplify the training effect and lead to localized heavy rainfall, which warrants closer attention in routine forecast operations.

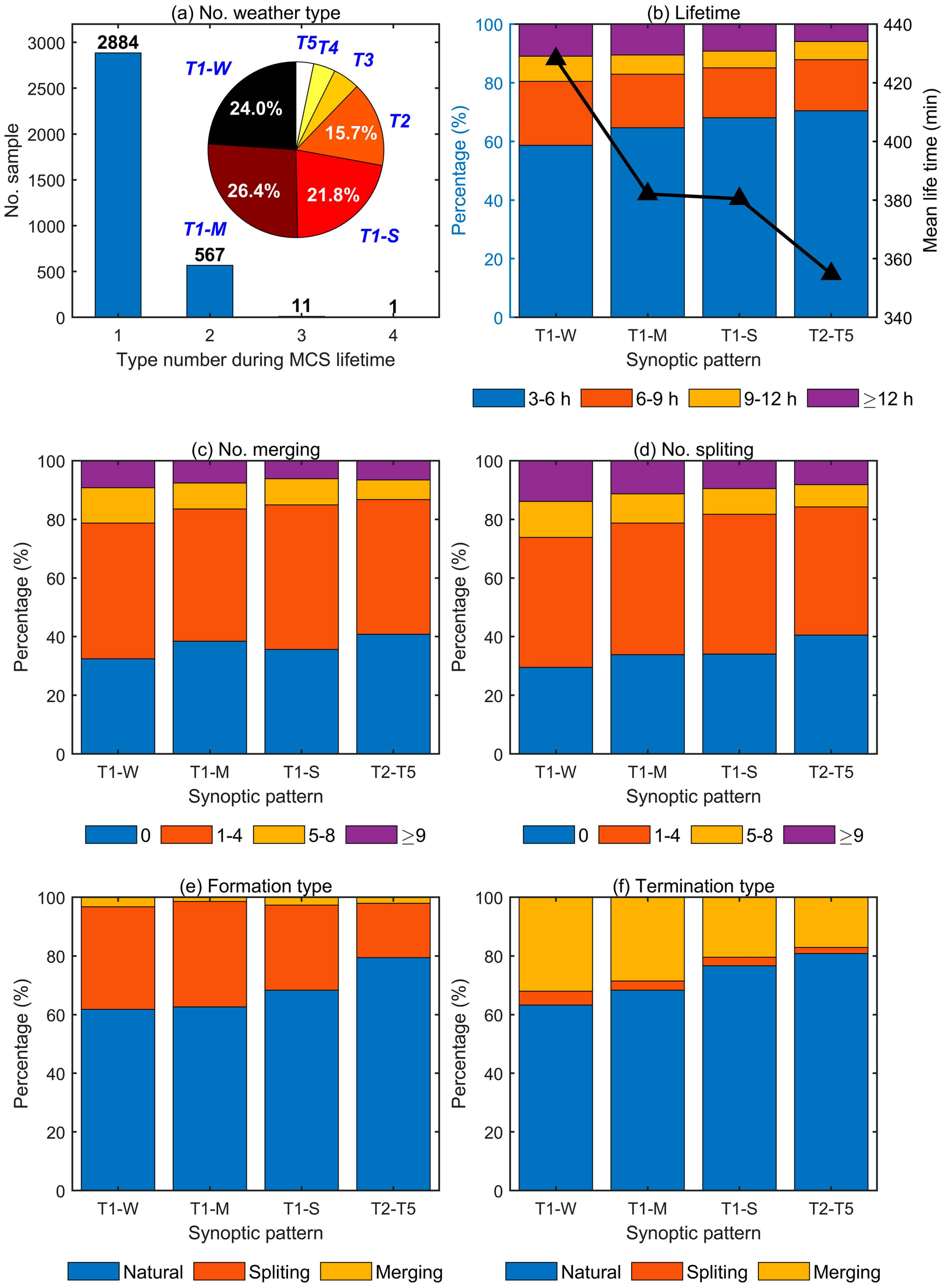

FIG. 9. MCS life cycle traits, including (a) the coverage number of WPSH synoptic types for all identified MCSs (shown in bar charts), with the percentages of one-type MCSs for different WPSH types (shown in a pie chart); (b) MCS lifetime distribution and mean lifetime (black curve with triangle symbols) as a function of WPSH pattern; (c) MCS merging and (d) splitting number distributions as a function of WPSH pattern; and (e) MCS formation and (f) termination type distributions as a function of WPSH pattern.

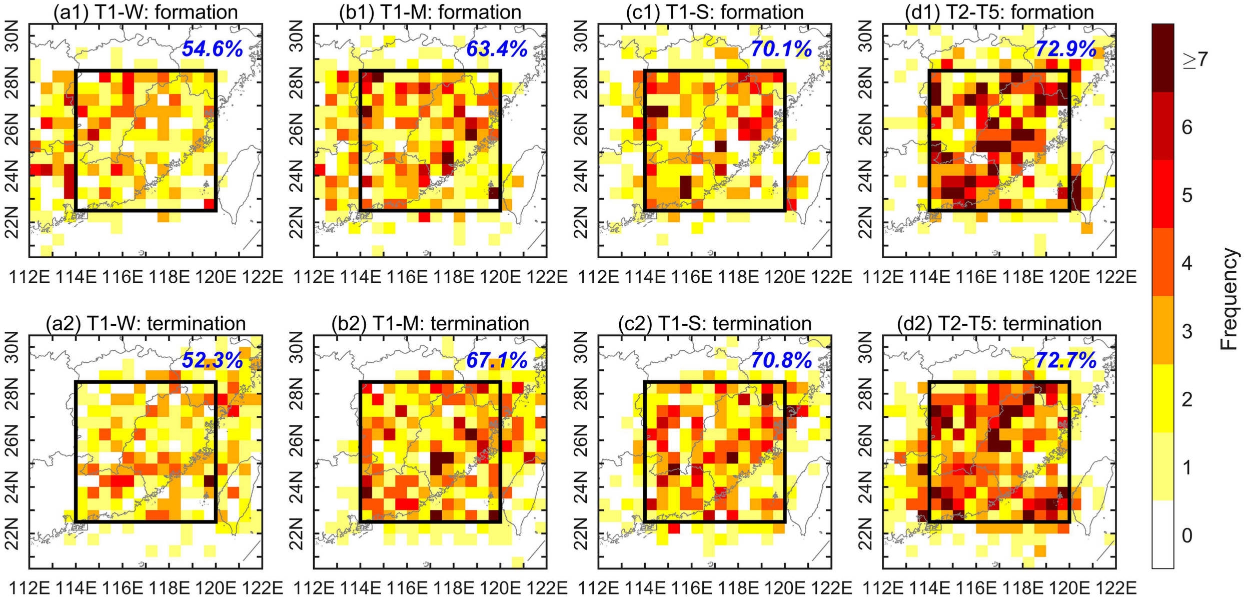

FIG. 10. Spatial distribution of the (a1)–(d1) formation and (a2)–(d2) termination sites of natural-type MCSs for different WPSH patterns. Provincial boundaries are denoted by gray curves. The black box denotes SEMC. The blue text in each panel shows the percentage of formation/termination sites within SEMC.

5. MCS-favorable environmental features in each WPSH pattern

While the differences in MCS features across various WPSH patterns have been explored, an important question remains: How do the environmental factors that favor MCS occurrence differ from those that inhibit it within each WPSH pattern? To address this, WPSH days in each synoptic type were divided into two groups for comparison: MCS-active days and MCS-inactive days. An MCS-active day was defined as one where the mean of hourly MCS fractions over SEMC exceeds the median value for its corresponding synoptic type. In contrast, an MCS-inactive day was defined as one where the mean MCS fraction falls below the median.

a. Synoptic-scale disturbances

Composite anomalies of 500-hPa vertical velocity, 700-hPa wind, and 700-hPa moisture flux on MCS-active days, relative to the mean state of their respective synoptic type (as shown in

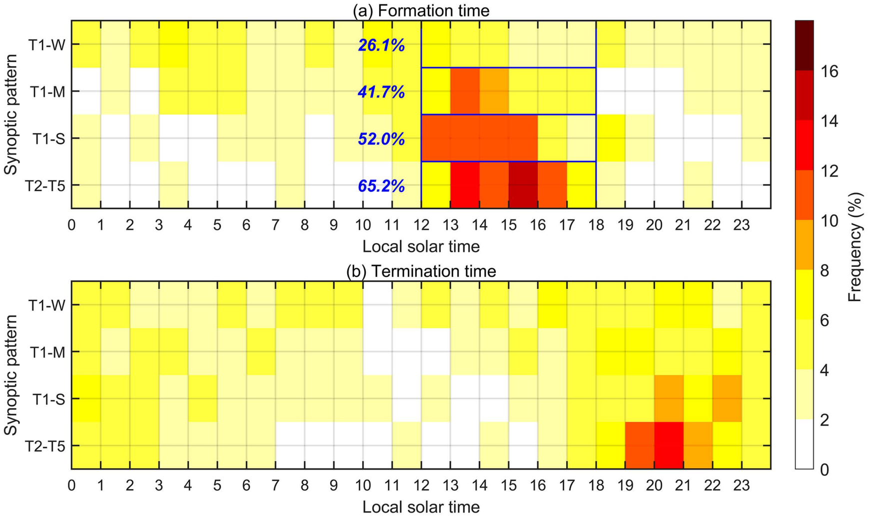

FIG. 11. Diurnal variation of the (a) formation and (b) termination times of natural-type MCSs within SEMC as a function of WPSH pattern. The blue text in (a) denotes the cumulative frequency of MCSs with formation times between 1200 and 1800 LST (blue box) for each WPSH pattern.

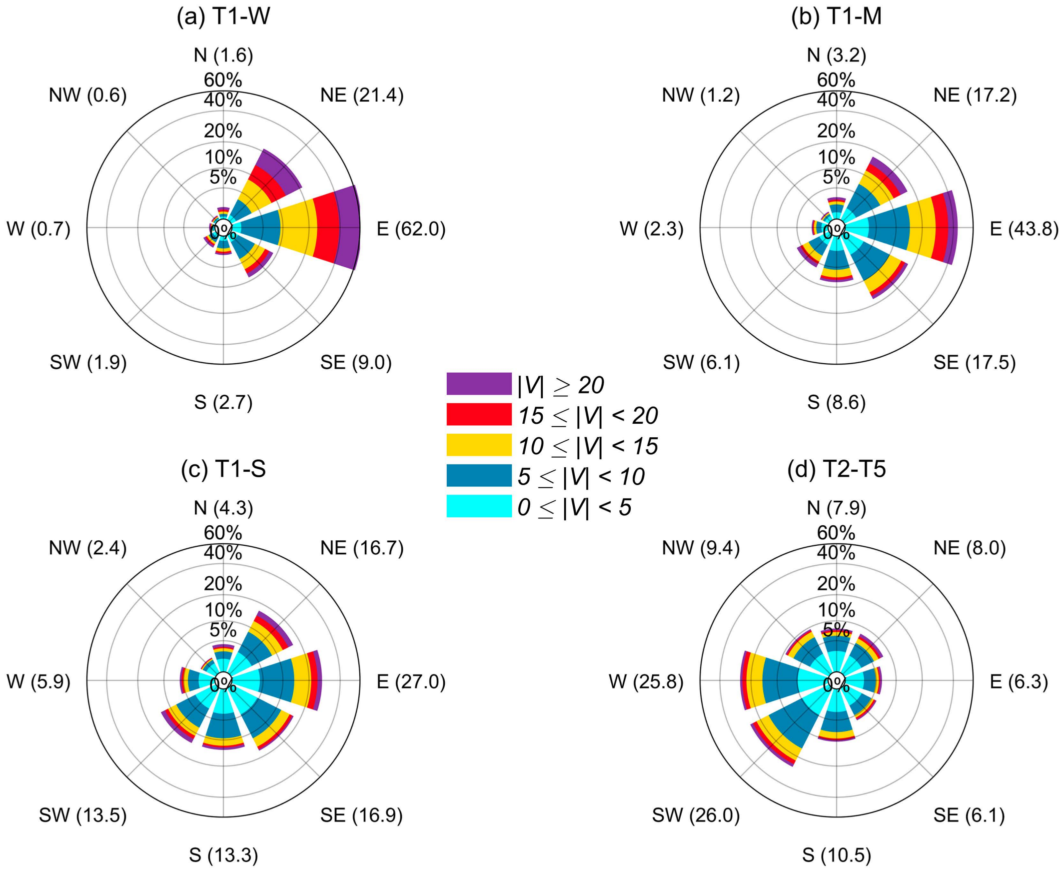

FIG. 12. Wind rose diagram showing the distribution of moving direction and speed for MCS samples with a natural continuity process, as a function of WPSH pattern. In each panel, the numbers in parentheses represent the percentages of MCS samples moving toward a specific direction.

Fig. 4), were investigated to demonstrate the role of synoptic-scale disturbances in various synoptic types. In the WPSH-periphery types, additional southwesterly and/or southerly components at 700 hPa, along with enhancing low-level moisture, provide anomalous moisture fluxes over SEMC on MCS-active days (Figs. 15a,b). Moreover, anomalous upward motions at 500 hPa are observed during these days. These findings suggest that enhanced synoptic-scale disturbances play a significant role in the active occurrence of MCSs in the WPSH-periphery types. Overall, the anomalous features are more pronounced in T1-W than in T1-M, with greater anomaly magnitudes and more extensive anomaly areas that pass the Student's *t* test.

In stark contrast to the WPSH-periphery types, the WPSH-center types show no significant signals of synoptic-scale disturbances for MCS occurrence (Figs. 15c–g). On MCS-active days, no significant anomalies are observed within SEMC for low-level winds or midlevel vertical motions in the WPSH-center types. One exception is the small area of enhanced moisture fluxes within SEMC in T1-S, T2, and T3. This enhancement is primarily caused by a significant increase in low-level specific humidity on MCS-active days, rather than changes in low-level winds. In fact, the low-level winds in the WPSH-center types are generally weaker on MCS-active days than the mean state, although the difference does not pass the significance test. The relatively calm environment within the WPSH center allows for the local accumulation of warm, moist air (Zeng et al. 2019). This process may be a key mechanism driving MCS occurrence in the WPSH-center scenario.

b. *Convective parameters*

We further examined the differences in convective parameters between MCS-active days and MCS-inactive days, in terms of CAPE, TCW, and KI. In addition to 0800 LST, the time of 1400 LST (just before the peak occurrence of MCSs from a diurnal view) is also included to account for the diurnal variations in convective parameters. The convective parameters across SEMC are weighted by the occurrence frequency of MCSs within the corresponding synoptic type to generate a weighted value for comparison. Using the weighted value allows for emphasizing the role of convective parameters near the MCS hotspots, which is more representative than using the mean value across entire SEMC.

As expected, all three convective parameters effectively distinguish MCS-active days from MCS-inactive days for both the WPSH-periphery and WPSH-center patterns (Fig. 16). The weighted CAPE, TCW, and KI consistently show significantly

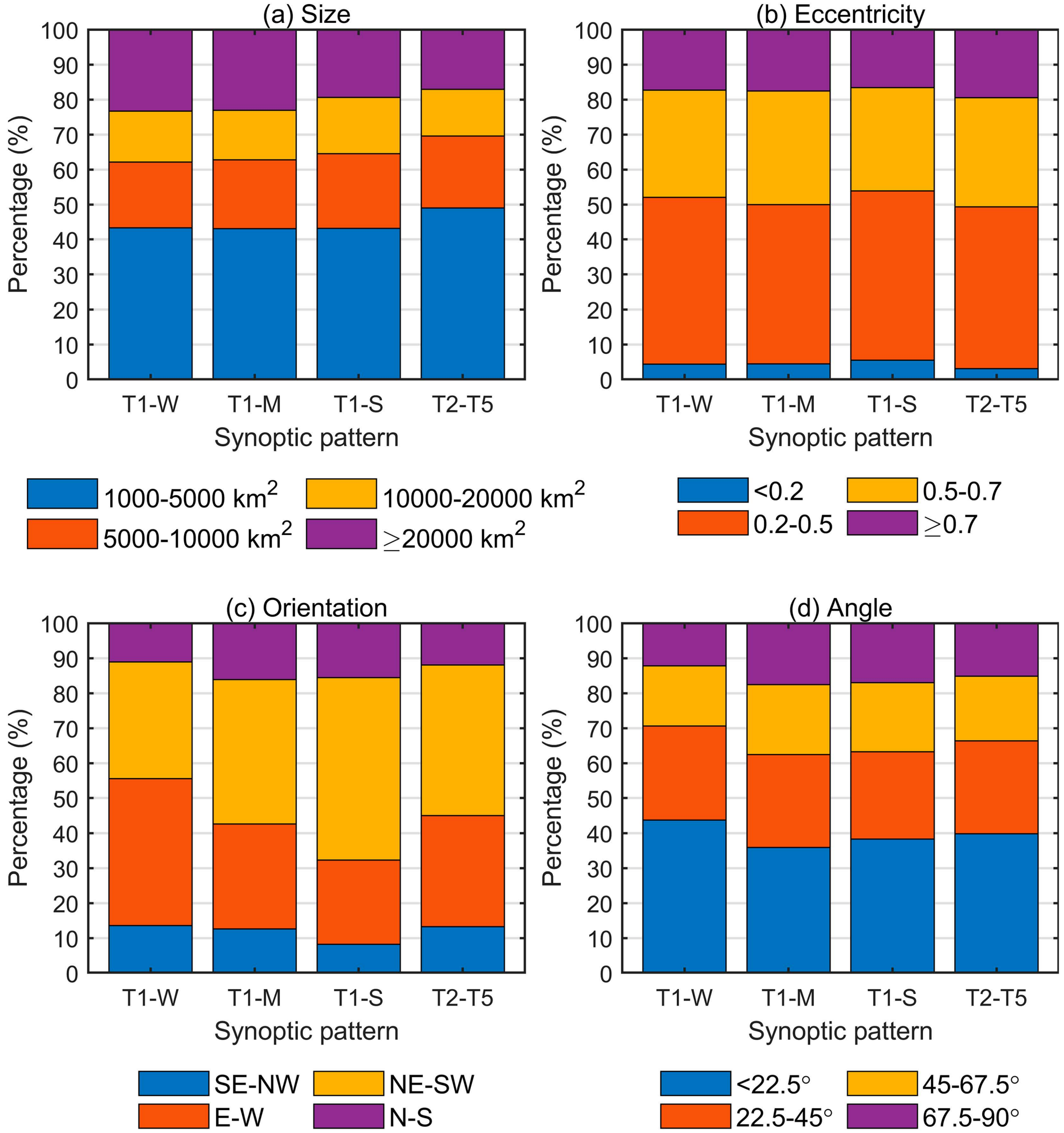

FIG. 13. Distribution of (a) size, (b) eccentricity, (c) orientation, and (d) angle between orientation and moving direction of MCSs, as a function of WPSH pattern.

higher medians on MCS-active days compared to MCS-inactive days, as indicated by the absence of overlap between the notches of the corresponding box plots. For example, at 1400 LST, the median values for the MCS-inactive days versus MCS-active days are 79–525 J kg^{-1} versus 705–984 J kg^{-1} for CAPE, 39–47 kg m^{-1} versus 49–55 kg m^{-1} for TCW, and 29–31 K versus 33–34 K for KI. These results suggest that favorable thermodynamic conditions—characterized by sufficient instability and moisture—are required for the active occurrence of MCSs, regardless of whether in the WPSH-periphery patterns or WPSH-center patterns. Notably, T1-W, the pattern with the strongest synoptic forcing, requires the least CAPE, TCW, and KI.

Among the three parameters, CAPE shows the most pronounced diurnal variation, particularly in the WPSH-periphery patterns (Fig. 16a). On MCS-active days, the median value increases by 1.8 times in T1-W (from 388 to 705 J kg^{-1}) and by 1.6 times in T1-M (from 589 to 946 J kg^{-1}) from 0800 to 1400 LST. In contrast, the WPSH-center patterns exhibit higher median CAPE values at 0800 LST, with relatively moderate increases by 1400 LST—only 1.3 times in T1-S and 1.2 times in T2–T5. This suggests that MCSs in the WPSH-center patterns tend to develop from a more unstable environment in the morning, whereas in the WPSH-periphery patterns, instability increases more notably throughout the day. Although the CAPE values on MCS-inactive days are generally lower than on MCS-active days, the diurnal variation patterns remain similar.

Regarding TCW (Fig. 16b) and KI (Fig. 16c), the increase from 0800 to 1400 LST is relatively small, with changes of no more than 2 kg m^{-1} and 3 K, respectively. This pattern holds true for

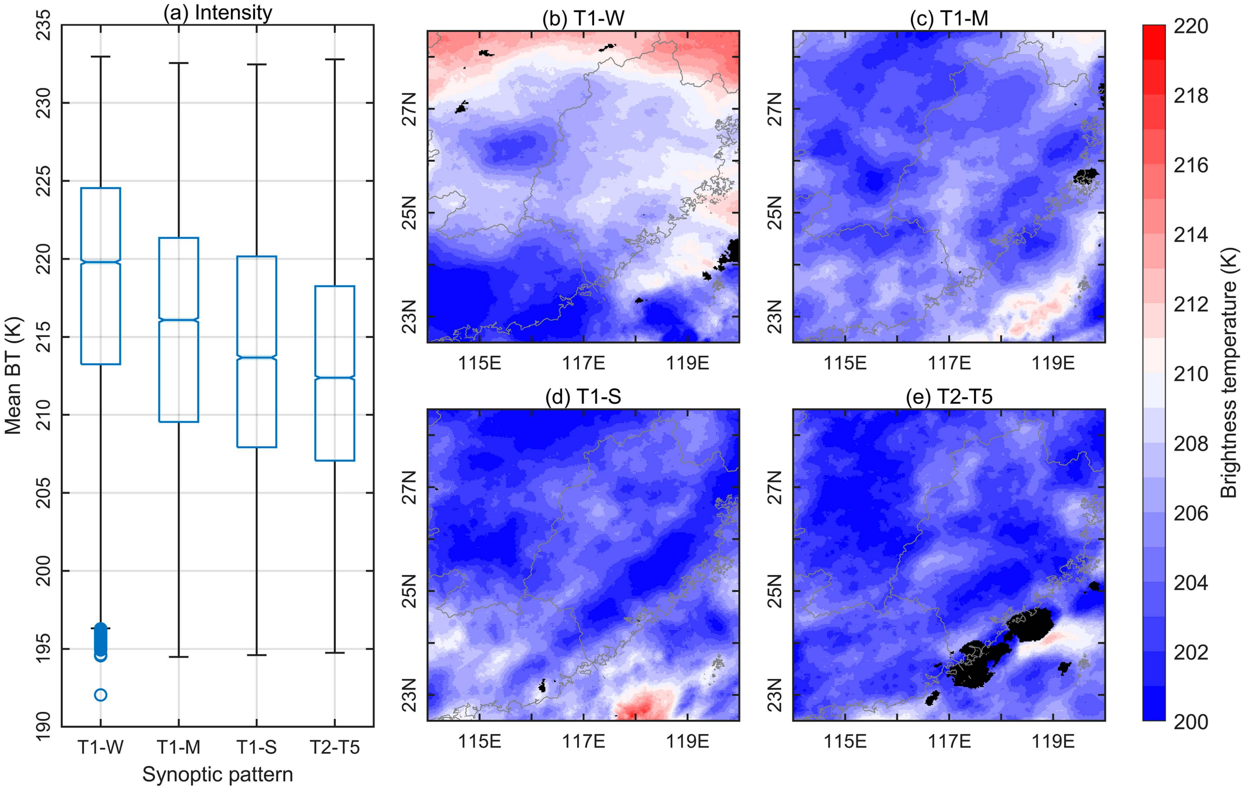

FIG. 14. Intensity comparison of MCSs over SEMC among different WPSH patterns using satellite-observed BTs, in terms of (a) box-and-whisker plots (refer to Fig. 3 for the plot style) of the mean BTs of the 10% coldest MCS pixels for each MCS sample and (b)–(e) spatial distribution of the mean BTs of the 10% coldest MCS pixels in each SEMC grid. The black areas in (b)–(e) represent regions where the mean BTs exhibit a large standard deviation (greater than 5 K), and these areas were excluded from the analysis. Provincial boundaries in (b)–(e) are denoted by gray curves.

both MCS-active and MCS-inactive days across all four patterns. A notable feature in these two parameters is the narrower distribution around higher values on MCS-active days compared to MCS-inactive days, especially for the WPSH-center patterns at 1400 LST. This highlights that sufficient local moisture and low-level instability are key prerequisites for MCS development in these conditions.

6. Summary and discussion

As a crucial globally existing weather system, subtropical highs have received extensive attention due to their impacts on large-scale weather and climate. However, our understanding of the linkage between the subtropical highs and mesoscale convective weather remains limited, hindering the improvement of convective weather forecasts in subtropical-high-involved scenarios. This study aims to explore the general characteristics of warm-season MCSs in response to variations in the WPSH pattern over SEMC, the region most frequently affected by the WPSH in the Asian continent, with emphasis on the comparison of MCS groups occurring at the WPSH periphery and center.

A total of 725 WPSH days were identified over SEMC, accounting for 56.6% of the seven warm seasons between 2016 and 2022. The synoptic circulations during WPSH days were classified into five typical types (T1–T5) through T-mode PCA, characterized by distinct positions of the WPSH center relative to SEMC. The most prevalent type, T1, was further subdivided into three subtypes based on WPSH intensity over SEMC: weak (T1-W), moderate (T1-M), and strong (T1-S). In general, T1-W and T1-M correspond to the WPSH-periphery patterns, where SEMC lies to the northwest of the WPSH center, while T1-S and T2–T5 represent the WPSH-center patterns, with SEMC located directly under the WPSH influence. The WPSH-periphery patterns are most common in early summer (April–June), while the WPSH-center patterns prevail in late summer (July–September).

During WPSH days, 3463 MCSs were identified over SEMC from successive infrared images taken by the *Himawari-8* satellite. These MCSs are most active over the north-central part of SEMC, particularly between the two highest mountains, with an occurrence frequency reaching up to 6%. MCS activity is notably higher in the WPSH-periphery patterns, where southwesterly jet streams bring abundant moisture into SEMC. The MCS hotspot shows a clear northward shift as the WPSH, and southwesterly jets move northward from T1-W to T1-M. In T1-W, two MCS hotspots are observed: one in the north-central region and another in the southwest, corresponding to frontal and warm-sector scenarios that are typical of early summer in southern

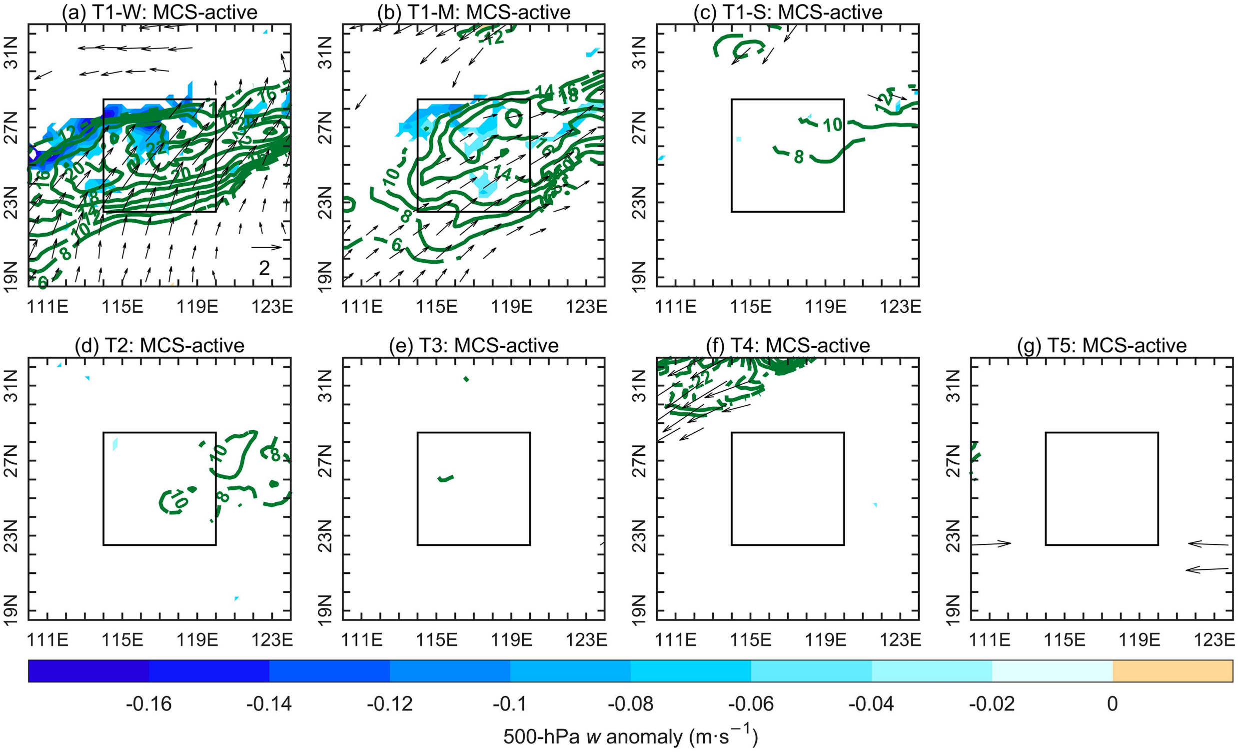

FIG. 15. Composite anomalies of MCS-active days relative to the mean state (shown in Fig. 4) for different WPSH types, showing 500-hPa vertical velocity (shading; m s^{-1}), 700-hPa winds (vectors; m s^{-1}), and 700-hPa moisture fluxes (contours; g kg^{-1} m s^{-1}). The composite anomalies are displayed only when they pass the Student's *t* test at a 90% confidence level. The black box in each panel denotes SEMC.

China. In the WPSH-center patterns, MCSs occur in a warm, moist environment with weaker synoptic forcing. These MCSs show a generally moderate frequency and more diverse hotspots compared to the WPSH-periphery patterns, though they remain significant, especially in hotspots with considerable occurrence frequency.

The different synoptic patterns consistently exhibit a single peak in MCS occurrence within the diurnal cycle, with the peak hour occurring between 1600 and 1900 LST. However, the diurnal amplitude is much larger in the WPSH-center patterns compared to the WPSH-periphery patterns. This suggests that MCSs at the WPSH center are more concentrated around the peak period, rather than occurring throughout the day. During the active period, MCS frequency in the WPSH-center patterns is comparable with or even higher than their WPSH-periphery counterparts. It is therefore speculated that MCS occurrence within the WPSH center is more strongly influenced by the thermodynamic effects with apparent diurnal cycle.

Longer MCS lifetimes are generally observed in the WPSH-periphery patterns compared to the WPSH-center patterns. This is accompanied by more frequent MCS merging and splitting processes in the WPSH-periphery patterns. MCSs in the WPSH-center patterns tend to form and terminate more naturally than their WPSH-periphery counterparts, with less involvement of merging or splitting. Spatially, MCS formation at the WPSH center is more concentrated within SEMC, particularly in the central mountainous regions. Temporally, MCSs in the WPSH-center patterns are more likely to form in the afternoon between 1200 and 1800 LST.

MCSs across different WPSH patterns show little variation in size and shape when observed from satellite cloud imagery. However, their movement and orientation exhibit significant differences, driven by the varying environmental flows in each pattern. Notably, the concurrent changes in movement direction and orientation form small angles with one another, which favor the development of the MCS training effect in both the WPSH-periphery and WPSH-center patterns. Compared to the WPSH-periphery patterns, the WPSH-center patterns are characterized by slower-moving MCSs with stronger intensity. This combination of features within the WPSH center could enhance the training effect, leading to higher potential of localized heavy rainfall production, making it an important consideration for routine forecasting.

The active occurrence of MCSs in the WPSH-periphery patterns is driven by anomalous synoptic disturbances, characterized by enhanced southwesterly/southerly jet streams, moisture transport, and midlevel upward motion. These features are absent in the WPSH-center patterns, where MCS activity occurs without significant synoptic-scale forcing. The examined convective parameters—CAPE, TCW, and KI—all effectively distinguish MCS-active days from inactive ones in both scenarios.

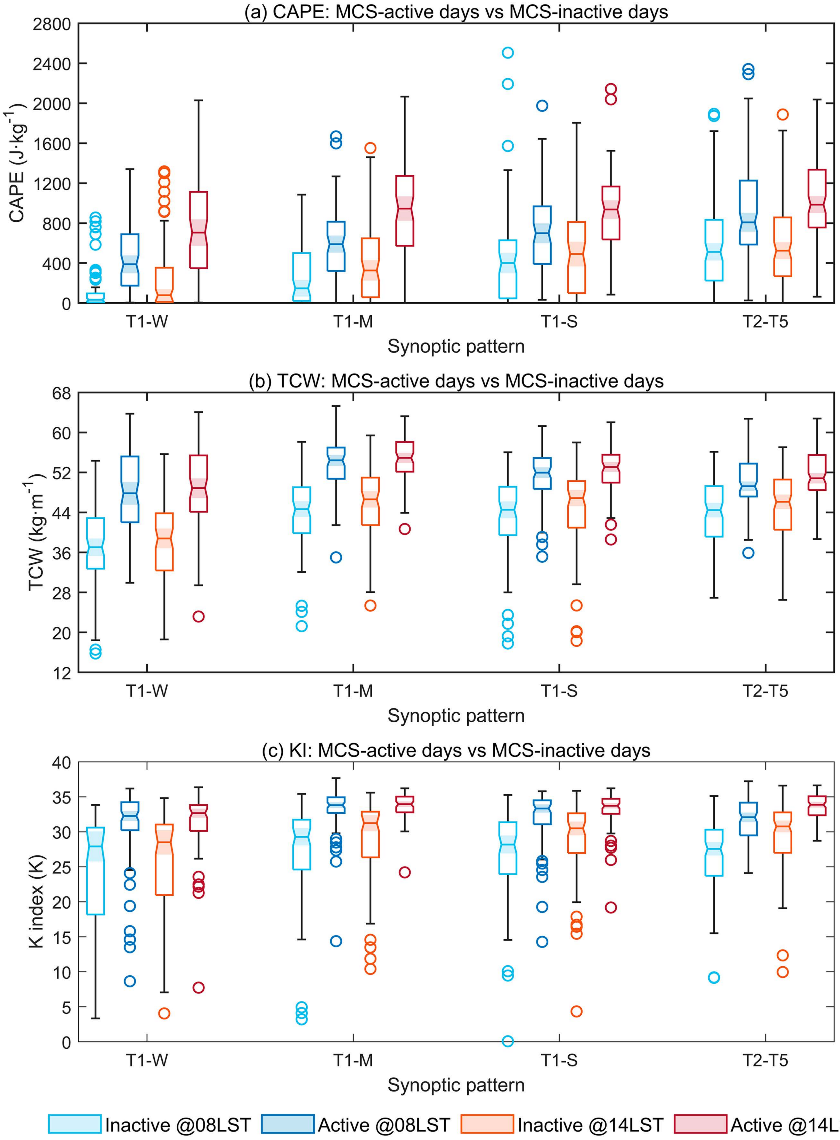

FIG. 16. Comparison of convective parameters, including (a) CAPE, (b) TCW, and (c) KI, between MCS-active days and MCS-inactive days at 0800 and 1400 LST for different WPSH patterns. The data are presented as box-and-whisker plots (refer to Fig. 3 for the plot style). Note that the values are weighted by the occurrence frequency of MCSs within the corresponding synoptic type to emphasize the influence of convective parameters near the MCS hotspots.

MCSs in the WPSH-center patterns typically form in a high-CAPE environment in the morning, whereas in the WPSH-periphery patterns, MCSs arise as instability increases significantly from morning to afternoon.

This study highlights the distinct behaviors and environmental features of warm-season MCSs occurring at the WPSH periphery and center, which are summarized in the schematics (Fig. 17). The results reveal that MCSs within the WPSH center are more frequent than traditionally expected and thus deserve the same level of attention as those occurring at the WPSH periphery. This is especially relevant since MCSs within the WPSH center have a high potential for generating the MCS training effect and often occur in weak synoptic-forcing environments of poor predictability. Given that the WPSH has been shown to extend westward under global warming (Cherchi et al. 2018; Zhou et al. 2009), the insights gained here regarding the relationship between the WPSH pattern and MCS characteristics are crucial not only for immediate forecasting of convective storms over SEMC but also for understanding future trends of MCSs in response to climate change. Future work will focus on comparing MCS-producing convective weather (especially heavy rainfall)

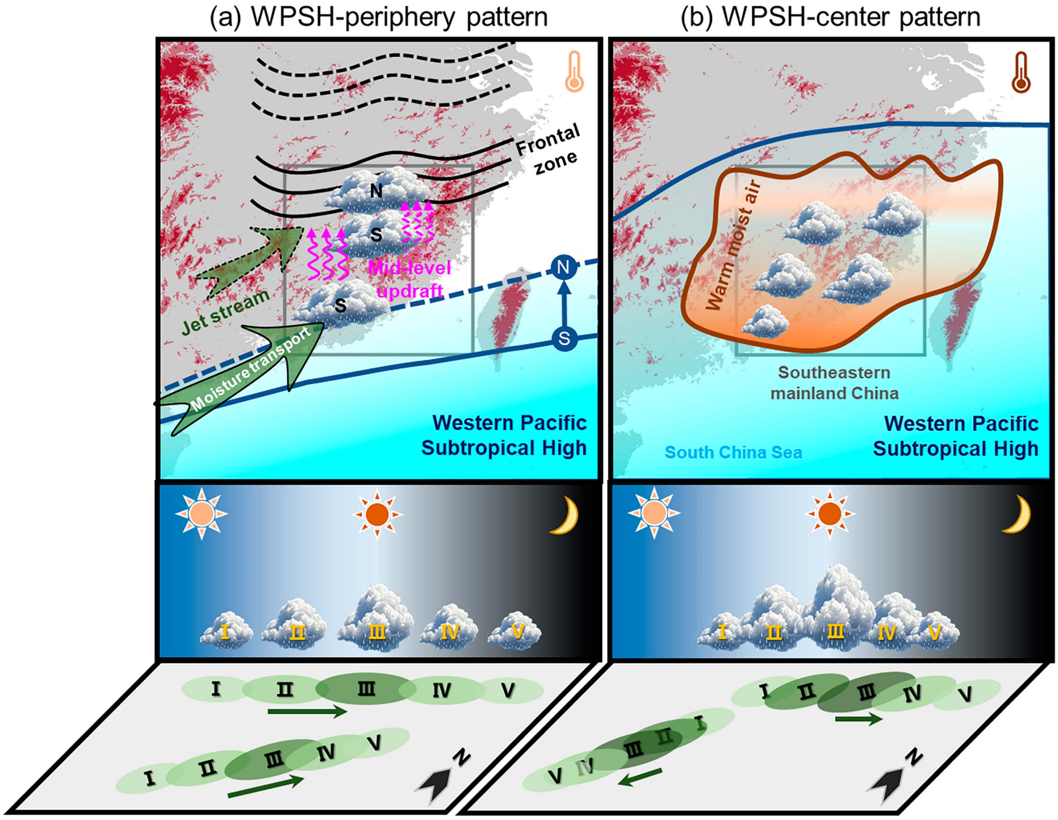

FIG. 17. Summary schematic diagram of the distinct characteristics of satellite-viewed warm-season MCSs over SEMC between the (a) WPSH-periphery pattern and (b) WPSH-center pattern. (top) The MCS hotpots (larger clouds indicate higher frequency) within each pattern, along with associated environmental features. (middle) The typical life cycle evolution of MCSs from a diurnal view (higher clouds indicate stronger intensity). (bottom) The typical propagation modes of MCSs corresponding to the five stages in (middle), with darker green color indicating higher potential of rainfall due to stronger MCS intensity.

across different WPSH patterns. It will also investigate localized mechanisms promoting MCS development within the WPSH center, such as land–sea contrast and the complex terrain of SEMC.

Acknowledgments. This work was sponsored by the National Natural Science Foundation of China (Grant 42305001), the Natural Science Foundation of Fujian Province (Grant 2023J011338), the National Natural Science Foundation of China (Grants 41905049, 42030604, 42475003, and 42275006), the Open Project of Xiamen Key Laboratory of Straits Meteorology (Grants HXQX202304 and 2024KF02), and the Fundamental Research Funds for the Central Universities (Grant 20720240029). We also appreciate the support from Fujian Meteorological Bureau Youth Team Foundation "Application of new-generation geostationary satellite on the severe convection over Taiwan Strait area."

Data availability statement. *Himawari-8* data can be obtained via the P-Tree system of the Japan Aerospace Exploration Agency at https://www.eorc.jaxa.jp/ptree/index.html. The ERA5 reanalysis data were provided by ECMWF and downloaded from Copernicus Climate Change Service Climate Data Store at https://cds.climate.copernicus.eu. The CMA tropical cyclone best track dataset was provided by CMA tropical cyclone data center at https://tcdata.typhoon.org.cn.

APPENDIX A

Diurnal Variation in the Spatial Distribution of MCS Occurrence Frequency for Different WPSH Patterns

Figure A1 shows the spatial distribution of the occurrence frequency of MCSs for different WPSH patterns at 3-h intervals.

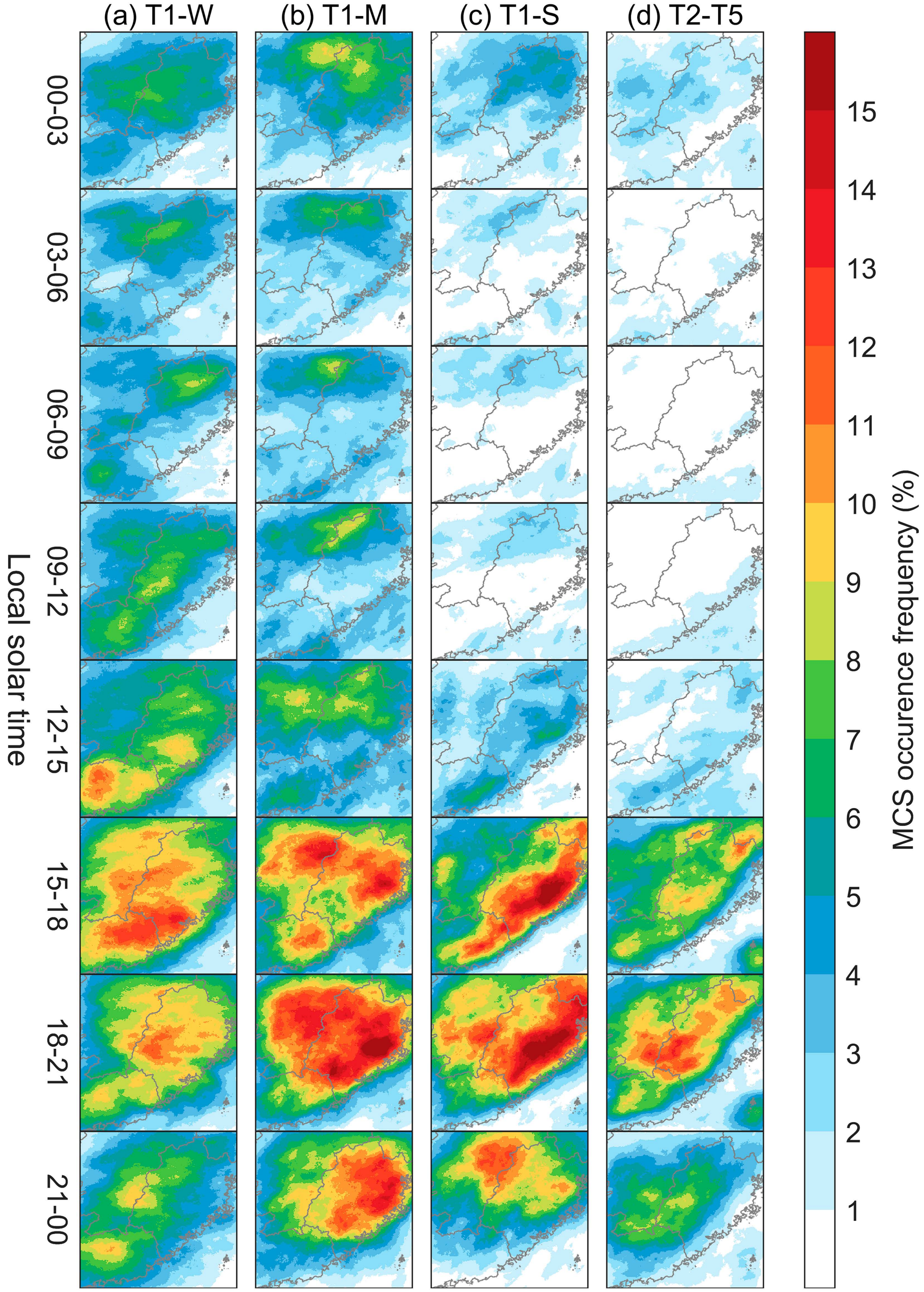

FIG. A1. Spatial distribution of the occurrence frequency of MCSs for different WPSH patterns at 3-h intervals. Provincial boundaries are denoted by gray curves.

APPENDIX B

Example of MCS Evolution on Two Representative Days for WPSH-Periphery and WPSH-Center Patterns

Figure B1 displays the infrared cloud images of the MCS evolution in SEMC on 2 days that were selected to represent WPSH-periphery and WPSH-center patterns.

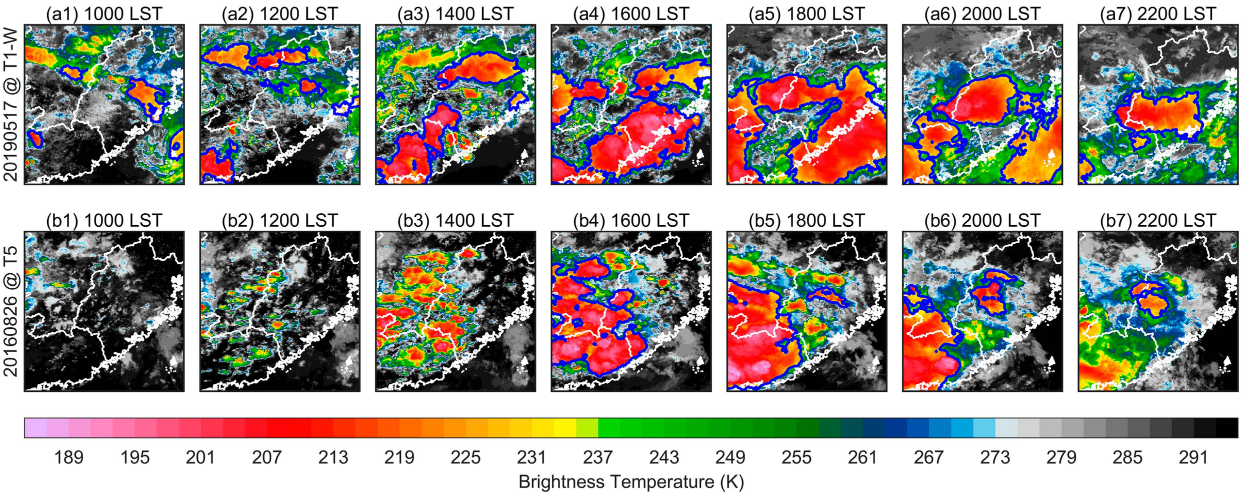

FIG. B1. Infrared cloud images derived from *Himawari-8* showing the evaluation of identified MCSs (blue contours) occurring in SEMC on (a1)–(a7) 17 May 2019 with a WPSH-periphery pattern (T1-W) and (b1)–(b7) 26 Aug 2016 with a WPSH-center pattern (T5). Provincial boundaries are denoted by white curves. The 2 days were selected as the representative days due to their averaged 500-hPa geopotential height over SEMC are around the median in their respective WPSH type.

REFERENCES

Bai, L., G. Chen, Y. Huang, and Z. Meng, 2021: Convection initiation at a coastal rainfall hotspot in South China: Synoptic patterns and orographic effects. *J. Geophys. Res. Atmos.*, **126**, e2021JD034642, https://doi.org/10.1029/2021JD034642.

Bessho, K., and Coauthors, 2016: An introduction to Himawari-8/9—Japan's new-generation geostationary meteorological satellites. *J. Meteor. Soc. Japan*, **94**, 151–183, https://doi.org/10.2151/jmsj.2016-009.

Chen, D., and Coauthors, 2019: Mesoscale convective systems in the Asian monsoon region from advanced Himawari Imager: Algorithms and preliminary results. *J. Geophys. Res. Atmos.*, **124**, 2210–2234, https://doi.org/10.1029/2018JD029707.

Cherchi, A., T. Ambrizzi, S. Behera, A. C. V. Freitas, Y. Morioka, and T. Zhou, 2018: The response of subtropical highs to climate change. *Curr. Climate Change Rep.*, **4**, 371–382, https://doi.org/10.1007/s40641-018-0114-1.

Ding, Y., and C. L. C. Johnny, 2005: The East Asian summer monsoon: An overview. *Meteor. Atmos. Phys.*, **89**, 117–142, https://doi.org/10.1007/s00703-005-0125-z.

——, Y. Liu, and Z.-Z. Hu, 2021: The record-breaking mei-yu in 2020 and associated atmospheric circulation and tropical SST anomalies. *Adv. Atmos. Sci.*, **38**, 1980–1993, https://doi.org/10.1007/s00376-021-0361-2.

Feng, S., and Y.-F. Fu, 2009: Seasonal characteristics of precipitation occurrences in the core area of the subtropical high. *Acta Meteor. Sin.*, **23**, 681–690.

——, Q. Liu, and Y.-F. Fu, 2011: Cloud variations under subtropical high conditions. *Adv. Atmos. Sci.*, **28**, 623–635, https://doi.org/10.1007/s00376-010-9194-0.

Feng, Z., L. R. Leung, S. Hagos, R. A. Houze, C. D. Burleyson, and K. Balaguru, 2016: More frequent intense and long-lived storms dominate the springtime trend in central US rainfall. *Nat. Commun.*, **7**, 13429, https://doi.org/10.1038/ncomms13429.

——, and Coauthors, 2021: A global high-resolution mesoscale convective system database using satellite-derived cloud tops, surface precipitation, and tracking. *J. Geophys. Res. Atmos.*, **126**, e2020JD034202, https://doi.org/10.1029/2020JD034202.

Guan, W., H. Hu, X. Ren, and X.-Q. Yang, 2019: Subseasonal zonal variability of the western Pacific subtropical high in summer: Climate impacts and underlying mechanisms. *Climate Dyn.*, **53**, 3325–3344, https://doi.org/10.1007/s00382-019-04705-4.

He, J., B. Zhou, M. Wen, and F. Li, 2001: Vertical circulation structure, interannual variation features and variation mechanism of western Pacific subtropical high. *Adv. Atmos. Sci.*, **18**, 497–510, https://doi.org/10.1007/s00376-001-0040-2.

Hersbach, H., and Coauthors, 2020: The ERA5 global reanalysis. *Quart. J. Roy. Meteor. Soc.*, **146**, 1999–2049, https://doi.org/10.1002/qj.3803.

Houze, R. A., Jr., 2018: 100 years of research on mesoscale convective systems. *A Century of Progress in Atmospheric and Related Sciences: Celebrating the American Meteorological Society Centennial*, *Meteor. Monogr.*, No. 59, Amer. Meteor. Soc., https://doi.org/10.1175/AMSMONOGRAPHS-D-18-0001.1.

——, K. L. Rasmussen, M. D. Zuluaga, and S. R. Brodzik, 2015: The variable nature of convection in the tropics and subtropics: A legacy of 16 years of the Tropical Rainfall Measuring Mission satellite. *Rev. Geophys.*, **53**, 994–1021, https://doi.org/10.1002/2015RG000488.

Hu, H., L. R. Leung, and Z. Feng, 2020: Observed warm-season characteristics of MCS and non-MCS rainfall and their recent changes in the central United States. *Geophys. Res. Lett.*, **47**, e2019GL086783, https://doi.org/10.1029/2019GL086783.

Huang, Y., and M. Zhang, 2022: Contrasting mesoscale convective system features of two successive warm-sector rainfall episodes in southeastern China: A satellite perspective. *Remote Sens.*, **14**, 5434, https://doi.org/10.3390/rs14215434.

——, Z. Meng, and M. Zhang, 2022a: Synoptic impacts on the occurrence of mesoscale boundaries and their associated convection over an area of sharp vegetation contrast. *Geophys. Res. Lett.*, **49**, e2022GL099449, https://doi.org/10.1029/2022GL099449.

——, M. Zhang, Y. Zhao, B. J.-D. Jou, H. Zheng, C. Luo, and D. Chen, 2022b: Inter-zone differences of convective development in a convection outbreak event over southeastern coast of China: An observational analysis. *Remote Sens.*, **14**, 131, https://doi.org/10.3390/rs14010131.

Huth, R., 1993: Ein beispiel für die anwendung der hauptkomponentenanalyse zur auffindung von zirkulationstypen über Europa. *Meteor. Z.*, **2**, 285–293, https://doi.org/10.1127/metz/2/1993/285.

——, C. Beck, A. Philipp, M. Demuzere, Z. Ustrnul, M. Cahynová, J. Kyselý, and O. E. Tveito, and, 2008: Classifications of atmospheric circulation patterns: Recent advances and applications. *Ann. N. Y. Acad. Sci.*, **1146**, 105–152, https://doi.org/10.1196/annals.1446.019.

Jirak, I. L., W. R. Cotton, and R. L. McAnelly, 2003: Satellite and radar survey of mesoscale convective system development. *Mon. Wea. Rev.*, **131**, 2428–2449, https://doi.org/10.1175/1520-0493(2003)131<2428:SARSOM>2.0.CO;2.

Laing, A. G., and J. M. Fritsch, 2000: The large-scale environments of the global populations of mesoscale convective complexes. *Mon. Wea. Rev.*, **128**, 2756–2776, https://doi.org/10.1175/1520-0493(2000)128<2756:TLSEOT>2.0.CO;2.

Lan, M., F. Huo, L. Zhou, S. Jiang, R. Cai, and J. Chen, 2022: Mechanisms of short-duration heavy rainfall in the western Pacific subtropical high area: An analysis of two rainstorms of 2018 in Hunan Province, China. *Atmos.–Ocean*, **60** (1), 1–12, https://doi.org/10.1080/07055900.2022.2060177.

Li, A., H. Yang, C. Cui, T. Peng, Y. Liao, M. Xu, and X. Wang, 2023: The 10 most influential heavy rain events in China in 2022: Selection and evaluation. *J. Meteor. Res.*, **37**, 908–918, https://doi.org/10.1007/s13351-023-3048-z.

Li, L., W. Li, and Y. Kushnir, 2012: Variation of the North Atlantic subtropical high western ridge and its implication to Southeastern US summer precipitation. *Climate Dyn.*, **39**, 1401–1412, https://doi.org/10.1007/s00382-011-1214-y.

Li, X., and Y. Du, 2021: Statistical relationships between two types of heavy rainfall and low-level jets in South China. *J. Climate*, **34**, 8549–8566, https://doi.org/10.1175/JCLI-D-21-0121.1.

Liu, B., C. Zhu, J. Su, S. Ma, and K. Xu, 2019: Record-breaking northward shift of the western North Pacific subtropical high in July 2018. *J. Meteor. Soc. Japan*, **97**, 913–925, https://doi.org/10.2151/jmsj.2019-047.

Lu, X., H. Yu, M. Ying, B. Zhao, S. Zhang, L. Lin, L. Bai, and R. Wan, 2021: Western North Pacific tropical cyclone database created by the China Meteorological Administration. *Adv. Atmos. Sci.*, **38**, 690–699, https://doi.org/10.1007/s00376-020-0211-7.

Mathon, V., H. Laurent, and T. Lebel, 2002: Mesoscale convective system rainfall in the Sahel. *J. Appl. Meteor.*, **41**, 1081–1092, https://doi.org/10.1175/1520-0450(2002)041<1081:MCSRIT>2.0.CO;2.

Meng, Z., D. Yan, and Y. Zhang, 2013: General features of squall lines in East China. *Mon. Wea. Rev.*, **141**, 1629–1647, https://doi.org/10.1175/MWR-D-12-00208.1.

Nesbitt, S. W., R. Cifelli, and S. A. Rutledge, 2006: Storm morphology and rainfall characteristics of TRMM precipitation features. *Mon. Wea. Rev.*, **134**, 2702–2721, https://doi.org/10.1175/MWR3200.1.

Nieto Ferreira, R., and T. M. Rickenbach, 2020: Effects of the North Atlantic subtropical high on summertime precipitation organization in the southeast United States. *Int. J. Climatol.*, **40**, 5987–6001, https://doi.org/10.1002/joc.6561.

Peixóto, J. P., and A. H. Oort, 1984: Physics of climate. *Rev. Mod. Phys.*, **56**, 365–429, https://doi.org/10.1103/RevModPhys.56.365.

Peters, J. M., and R. S. Schumacher, 2014: Objective categorization of heavy-rain-producing MCS synoptic types by rotated principal component analysis. *Mon. Wea. Rev.*, **142**, 1716–1737, https://doi.org/10.1175/MWR-D-13-00295.1.

Philipp, A., C. Beck, R. Huth, and J. Jacobeit, 2016: Development and comparison of circulation type classifications using the COST 733 dataset and software. *Int. J. Climatol.*, **36**, 2673–2691, https://doi.org/10.1002/joc.3920.

Ren, X., X.-Q. Yang, and X. Sun, 2013: Zonal oscillation of western Pacific subtropical high and subseasonal SST variations during Yangtze persistent heavy rainfall events. *J. Climate*, **26**, 8929–8946, https://doi.org/10.1175/JCLI-D-12-00861.1.

Schumacher, R. S., and R. H. Johnson, 2005: Organization and environmental properties of extreme-rain-producing mesoscale convective systems. *Mon. Wea. Rev.*, **133**, 961–976, https://doi.org/10.1175/MWR2899.1.

——, and K. L. Rasmussen, 2020: The formation, character and changing nature of mesoscale convective systems. *Nat. Rev. Earth Environ.*, **1**, 300–314, https://doi.org/10.1038/s43017-020-0057-7.

Shen, Y., A. Xiong, Y. Wang, and P. Xie, 2010: Performance of high-resolution satellite precipitation products over China. *J. Geophys. Res.*, **115**, D02114, https://doi.org/10.1029/2009JD012097.

Song, F., Z. Feng, L. R. Leung, R. A. Houze Jr., J. Wang, J. Hardin, and C. R. Homeyer, 2019: Contrasting spring and summer large-scale environments associated with mesoscale convective systems over the U.S. Great Plains. *J. Climate*, **32**, 6749–6767, https://doi.org/10.1175/JCLI-D-18-0839.1.

Su, T.-H., and F. Xue, 2015: Two northward jumps of the summertime western Pacific subtropical high and their associations with the tropical SST anomalies. *Atmos. Oceanic Sci. Lett.*, **4**, 98–102.

Taylor, C. M., and Coauthors, 2017: Frequency of extreme Sahelian storms tripled since 1982 in satellite observations. *Nature*, **544**, 475–478, https://doi.org/10.1038/nature22069.

Thomas, C. M., and D. M. Schultz, 2019: Global climatologies of fronts, airmass boundaries, and airstream boundaries: Why the definition of "front" matters. *Mon. Wea. Rev.*, **147**, 691–717, https://doi.org/10.1175/MWR-D-18-0289.1.

Trier, S. B., C. A. Davis, D. A. Ahijevych, and K. W. Manning, 2014: Use of the parcel buoyancy minimum ($B_{\min}$) to diagnose simulated thermodynamic destabilization. Part II: Composite analysis of mature MCS environments. *Mon. Wea. Rev.*, **142**, 967–990, https://doi.org/10.1175/MWR-D-13-00273.1.

Vila, D. A., L. A. T. Machado, H. Laurent, and I. Velasco, 2008: Forecast and Tracking the Evolution of Cloud Clusters (ForTraCC) using satellite infrared imagery: Methodology and validation. *Wea. Forecasting*, **23**, 233–245, https://doi.org/10.1175/2007WAF2006121.1.

Wang, C., K. Zhao, A. Huang, X. Chen, and X. Rao, 2021: The crucial role of synoptic pattern in determining the spatial distribution and diurnal cycle of heavy rainfall over the South China coast. *J. Climate*, **34**, 2441–2458, https://doi.org/10.1175/JCLI-D-20-0274.1.

Wu, N., X. Ding, Z. Wen, G. Chen, Z. Meng, L. Lin, and J. Min, 2020: Contrasting frontal and warm-sector heavy rainfalls over South China during the early-summer rainy season. *Atmos. Res.*, **235**, 104693, https://doi.org/10.1016/j.atmosres.2019.104693.

Yang, X., J. Fei, X. Huang, X. Cheng, L. M. V. Carvalho, and H. He, 2015: Characteristics of mesoscale convective systems over China and its vicinity using geostationary satellite FY2. *J. Climate*, **28**, 4890–4907, https://doi.org/10.1175/JCLI-D-14-00491.1.

Yin, H., and X. Cao, 2010: Summary on subtropical high severe convection during midsummer in Shanghai area. *Meteor. Mon.*, **36**, 19–25.

Zeng, W., G. Chen, Y. Du, and Z. Wen, 2019: Diurnal variations of low-level winds and precipitation response to large-scale circulations during a heavy rainfall event. *Mon. Wea. Rev.*, **147**, 3981–4004, https://doi.org/10.1175/MWR-D-19-0131.1.

——, ——, L. Bai, Q. Liu, and Z. Wen, 2022: Multiscale processes of heavy rainfall over East Asia in summer 2020: Diurnal cycle in response to synoptic disturbances. *Mon. Wea. Rev.*, **150**, 1355–1376, https://doi.org/10.1175/MWR-D-21-0308.1.

Zhang, M., and Z. Meng, 2019: Warm-sector heavy rainfall in southern China and its WRF simulation evaluation: A low-level-jet perspective. *Mon. Wea. Rev.*, **147**, 4461–4480, https://doi.org/10.1175/MWR-D-19-0110.1.

——, K. L. Rasmussen, Z. Meng, and Y. Huang, 2022: Impacts of coastal terrain on warm-sector heavy-rain-producing MCSs in southern China. *Mon. Wea. Rev.*, **150**, 603–624, https://doi.org/10.1175/MWR-D-21-0190.1.

Zhou, T., and Coauthors, 2009: Why the western Pacific subtropical high has extended westward since the late 1970s. *J. Climate*, **22**, 2199–2215, https://doi.org/10.1175/2008JCLI2527.1.

Zuluaga, M. D., and R. A. Houze Jr., 2013: Evolution of the population of precipitating convective systems over the equatorial Indian Ocean in active phases of the Madden–Julian oscillation. *J. Atmos. Sci.*, **70**, 2713–2725, https://doi.org/10.1175/JAS-D-12-0311.1.